

Characterisation of $\text{La}_{0.75}\text{Sr}_{0.25}\text{Cr}_{0.50}\text{Mn}_{0.50}\text{O}_{3-\delta}$ (LSCM) redox-stable perovskite anodes for solid oxide fuel cells



Symmetric cells of LSCM on a TZ3Y electrolyte

R.H.F. Verhoeven
MSc thesis
March 2006
Inorganic Material Science
Faculty of Science and Technology
University of Twente
Enschede, the Netherlands



Characterisation of $\text{La}_{0.75}\text{Sr}_{0.25}\text{Cr}_{0.50}\text{Mn}_{0.50}\text{O}_{3-\delta}$ (LSCM) redox-stable perovskite anodes for solid oxide fuel cells

MSc thesis
by
R.H.F. Verhoeven

Graduation Committee

Prof. dr. ing. D.H.A. Blank

Chairman – Inorganic Material Science, University of Twente

Dr. B.A. Boukamp

Supervisor – Inorganic Material Science, University of Twente

Dr. H.J.M. Bouwmeester

Supervisor – Inorganic Material Science, University of Twente

Dr. F.P.F. van Berkel

ECN Fuel Cell Technology, Scientist SOFC, Petten

Dr. B.L. Mojet

Catalytic Processes and Materials, University of Twente

Abstract

In the search for alternative, environmental friendly and efficient power generation, the fuel cell is a promising option. There are several types of fuel cells. The Solid Oxide Fuel Cell (SOFC) is a high temperature fuel cell and it is a very efficient device for the electrochemical conversion of chemical energy into electricity.

Currently the mostly used anode materials for SOFC's are Ni/YSZ cermets. Ni/YSZ cermets have excellent catalytic properties and stability for hydrogen oxidation at SOFC operating conditions. However, these cermets do exhibit some disadvantages as low tolerance to sulphur and the deposition of carbon when using hydrocarbon fuels. Poor redox cycling is observed, causing volume instability and the nickel metal in the cermet tends to agglomerate after prolonged operation.

A possible alternative for this anode material is the usage of a ceramic perovskite structure. $\text{La}_{0.75}\text{Sr}_{0.25}\text{Cr}_{0.5}\text{Mn}_{0.5}\text{O}_{3-\delta}$ (LSCM) is stated in literature [Tao S., Irvine J.T.S., *Nature Materials*, 2, 2003] to be a possible alternative for Ni/YSZ cermets as anode material for solid oxide fuel cells.

This report describes the electrochemical characterisation of symmetric cells of LSCM on a TZ3Y electrolyte layer by using Electrochemical Impedance Spectroscopy (EIS). Electrode polarisation resistances of $0.37 - 1.12 \text{ Ohm}\cdot\text{cm}^2$ are found in different wet H_2/N_2 compositions at 850°C and values of 0.29 and $0.67 \text{ Ohm}\cdot\text{cm}^2$ are found in wet H_2 at 850°C . These results are obtained on a symmetric cell with LSCM electrodes sintered at 1200°C in air. These values are comparable with LSCM polarisation resistances stated in literature and are also close to conventionally Ni/YSZ cermet anodes polarisation resistances.

A conducting gold paste layer is applied on these electrode layers to increase the contact between the electrodes and platinum current collectors. Using a conducting gold layer is essential for impedance measurements on these symmetric cells. The lateral conductivity is therefore optimised, resulting in a representative measurement for the electrochemical performance of the electrode material.

The most important processes that take place in the anode material, contributing the most to the polarisation resistance, are surface processes. Typically dissociative adsorption of hydrogen on the anode surface is expected to take place, combined with gas transport limitation processes of gaseous species in the material.

Table of contents

1	INTRODUCTION	9
1.1	TYPES OF FUEL CELLS	9
1.2	SOLID OXIDE FUEL CELL	10
1.3	OBJECTIVE	11
2	THEORETICAL BACKGROUND	13
2.1	NI/YSZ ANODE MATERIALS	13
2.2	CU-CEO ₂ ANODE MATERIALS	14
2.3	PEROVSKITE ANODE MATERIALS	14
2.4	COMPARISON OF OTHER MATERIALS	15
2.5	ELECTROCHEMICAL IMPEDANCE SPECTROSCOPY	16
2.6	POLARISATION	17
3	EXPERIMENTAL	19
3.1	THE SET-UP	19
3.2	CLOSE-UP OF THE SAMPLE HOLDER	19
3.3	SAMPLE GEOMETRY AND COMPOSITION	20
3.4	MEASURING PROCEDURE	21
4	RESULTS AND DISCUSSION	23
4.1	LA _{0.75} SR _{0.25} CR _{0.5} MN _{0.5} O _{3-δ} SINTERED AT 1200 °C IN AIR	24
4.2	LA _{0.75} SR _{0.25} CR _{0.5} MN _{0.5} O _{3-δ} SINTERED AT 1500 °C IN AIR	29
4.3	LA _{0.75} SR _{0.25} CR _{0.5} MN _{0.5} O _{3-δ} SINTERED AT 1200 °C IN HYDROGEN	32
4.4	GOLD SPUTTERED AND GOLD PAINTED LSCM ELECTRODES	33
4.5	MEASUREMENTS AT INCREASED PO ₂	37
5	CONCLUSIONS AND RECOMMENDATIONS	39
6	DANKWOORD	41
7	LITERATURE	43
	APPENDICES	45

1 Introduction

A fuel cell is an energy conversion device that converts the chemical energy of a fuel directly to electrical energy and heat without the need for direct combustion as an intermediate step, giving much higher conversion efficiencies than conventional thermo-mechanical methods. The operating principles of fuel cells are similar to those of batteries. There is an electrochemical combination of reactants to generate electricity. The combination is made of a gaseous fuel (e.g. hydrogen) and an oxidant gas (oxygen) through electrodes and via an ion-conducting electrolyte.

However, unlike a battery, a fuel cell does not run down or require recharging. A fuel cell operates as long as both fuel and oxidant are supplied to the electrodes and the influence it exerts on the surrounding environment is negligible [1],[2].

1.1 Types of fuel cells

There are different types of fuel cells, each designed for different applications and needs, operating at different temperatures and efficiencies. The fuel cells are characterised by the material used as electrolyte. Table 1 gives a brief overview of available types of fuel cells.

Table 1: Technical characteristics of different fuel cells [1].

Type of fuel cell	Electrolyte	Operating Temp. (°C)	Fuel	Efficiency (%)
Alkaline Fuel Cell (AFC)	KOH NaOH	50-200	pure hydrogen or hydrazine	50-55
Direct Methanol Fuel Cell (DMFC)	polymer	60-200	liquid methanol	40-55
Phosphoric Acid Fuel Cell (PAFC)	Phosphoric acid H ₃ PO ₄	160-210	hydrogen from hydrocarbons, alcohol	40-50
Sulphuric Acid Fuel Cell (SAFC)	Sulphuric acid H ₂ SO ₄	80-90	alcohol or (impure) hydrogen	40-50
Proton Exchange Membrane Fuel Cell (PEMFC)	polymer membrane (e.g. Nafion® by DuPont)	50-80	less pure hydrogen from hydrocarbons or methanol	40-50
Molten Carbonate Fuel Cell (MCFC)	Li ₂ CO ₃ -K ₂ CO ₃ Li ₂ CO ₃ -Na ₂ CO ₃	630-650	hydrogen, carbon monoxide, natural gas, propane, marine diesel	50-60
Solid Oxide Fuel Cell (SOFC)	Yttria-stabilised zirconia (YSZ)	600-1000	hydrogen, carbon monoxide, natural gas, propane, marine diesel	45-60
Protonic Ceramic Fuel Cell (PCFC)	Barium cerium oxide	600-700	hydrocarbons	45-60

With these properties, each fuel cell is applied in different power ranges. For instance, alkaline fuel cells are generating power in the range of less than 5 kW and are therefore used in niche markets like the military or in space programs. PEM fuel cells are used in portable and automotive applications having a typical power range of 5 – 250 kW. Phosphoric acid fuel cells have a power range of around 200 kW and are used as stationary combined heat and power units. Molten carbonate and solid oxide fuel cells are both used as stationary combined heat and power units as well with power ranges of 200 kW – MW respectively 2 kW – MW [3].

1.2 Solid Oxide Fuel Cell

According to the definition, the Solid Oxide Fuel Cell (SOFC) has a solid oxide electrolyte material. The most common electrolyte structure is Ytria-Stabilized Zirconia (YSZ). Undoped zirconia (see Figure 1) exhibits three polymorphs. It has a monoclinic structure at room temperature, changing to tetragonal above 1170 °C and to the cubic fluorite structure above 2370 °C.

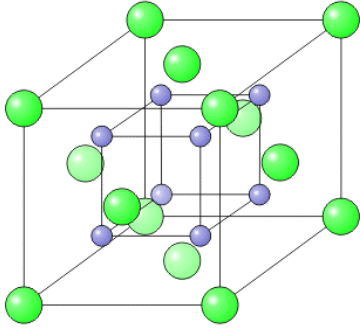


Figure 1: Crystal structure of cubic zirconia. The small atoms are oxygen atoms; the big atoms are zirconium atoms [4].

The addition of a dopant such as yttria stabilises the fluorite and tetragonal phases down to room temperature, leading to an increase in the oxygen vacancy concentration. This makes the material an excellent oxygen-ion conductor.

The electronic conductivity of YSZ is negligible compared to the ionic conductivity at operating conditions of the fuel cell [5]. This is necessary for the operating principles as discussed below.

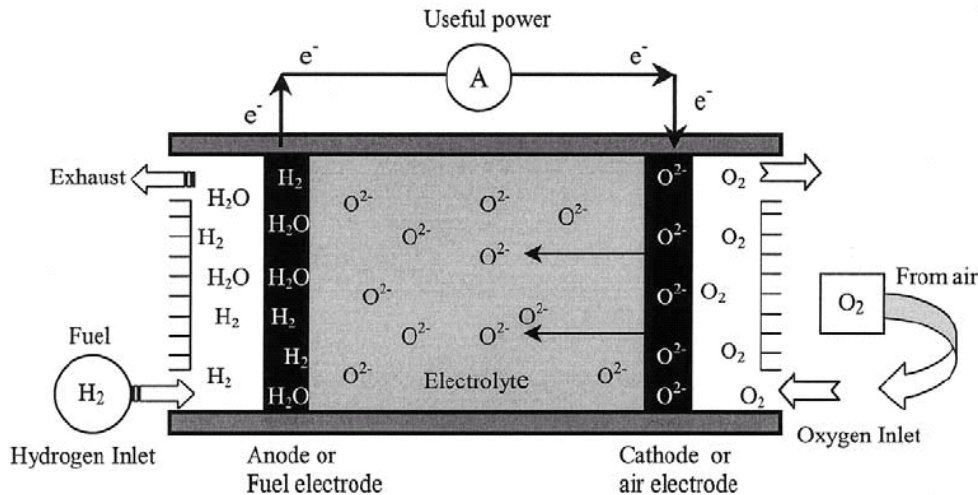


Figure 2: Principle of a solid oxide fuel cell based on oxygen-ion conductors [1].

Fuel (e.g. hydrogen) is fed to the anode side of the fuel cell where it is oxidised by oxygen ions that are transported through the electrolyte. Electrons are released to the external circuit. So at the anode side of the fuel cell the following reaction occurs:

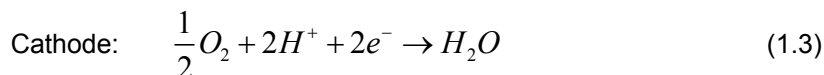


Oxidant (mostly oxygen or air) is fed to the cathode side of the fuel cell. The electrons are accepted from the external circuit and the oxygen is reduced to oxygen ions. The cathode reaction is given by:



The resulting oxygen ions are transported through the electrolyte and the external flow of electrons can be used to power a device.

Analogue to this principle, SOFCs can also be equipped with proton conducting solid oxide electrolytes. The accompanying electrode reactions are:



However, proton-conducting electrolytes are not in the scope of this work and will therefore not be discussed further.

YSZ is currently the mostly used electrolyte material for solid oxide fuel cells. Next, the cathode, anode and interconnect materials are shortly discussed.

Cathodes operate in a highly oxidising environment. Therefore it is not possible to use base metals as cathode material. Noble metals are better compatible with these kinds of environments but they are too expensive. Nowadays strontium doped lanthanum manganites (LSM) are mostly used as cathode material on YSZ electrolytes. Typically $La_{0.8}Sr_{0.2}MnO_3$ gives a good combination of electronic conductivity, matching thermal expansion coefficient with the electrolyte and it can withstand the oxidising environment successfully. Better conductivity can be reached by using higher dopant levels, but this has negative effects on the expansion coefficient. LSM is often mixed with YSZ in about a 50/50 relation to form a first layer of cathode material on the electrolyte. This increases the electrode/electrolyte active contacting surface [5].

Currently nickel-based composites are mostly used as anode material. However, nickel-based composite anodes have some practical issues during fuel cell operation. These problems, as well as available alternative anode materials, are extensively discussed in chapter 2.

The connection between anode and cathode for electron transportation is often combined into a single material that makes contact with both electrodes. So, this material has to withstand both oxidising and reducing environments. Also the operating temperature, the design of the cell and how they are placed in a stack is important in the choice for interconnect materials. For instance, magnesium doped lanthanum chromites are used by Siemens Westinghouse to produce single cells and stacks of their tubular design. Sulzer Hexis uses a coated alloy of chromium, iron and yttria. Adelan uses externally connected wires in their micro-tubular design [5].

The SOFC produces a significant amount of heat during operation. This heat is generated by the electrochemical reactions, ohmic losses, electrode overpotentials etc. The fuel cell itself operates at a temperature of 600 – 1000 °C, mainly to get the desired ion-conductivity of YSZ. A part of the generated heat can be used to keep the SOFC at operating temperature. The rest of the remaining heat can be used parallel to the power generation to increase the efficiency of the system. For instance, a residential SOFC system can use this heat to produce hot water. A stationary power system can use the hot exhaust gas from the SOFC to gasify coal or to drive a heat engine such as a Stirling engine or a gas turbine motor [3], [6]-[9].

1.3 Objective

Currently the mostly used anode materials for SOFC's are Ni/YSZ cermets. As discussed in paragraph 2.1 *Ni/YSZ anode materials*, these anodes experience quite some drawbacks in SOFC system operation. A possible alternative for this anode material is the usage of a ceramic perovskite structure, $La_{0.75}Sr_{0.25}Cr_{0.5}Mn_{0.5}O_{3-\delta}$ (LSCM), as anode material. In literature good results are demonstrated by using this ceramic perovskite as anode material [10], [11]. The objective of this research is to focus on a better characterisation of the electrochemical processes based on the redox stable perovskite anode. The results will be linked to existing or possibly new models for electrochemical processes. The anodes will be electrochemically characterised by using Electrochemical Impedance Spectroscopy (EIS).

2 Theoretical background

In solid oxide fuel cells, the anode is the electrode for the electrochemical oxidation of fuels such as hydrogen and natural gas. Hydrogen oxidation is one of the most important electrode reactions in solid oxide fuel cells. The electrochemical oxidation of hydrogen can be written in Kröger-Vink as:



To minimize the polarization losses of the H_2 oxidation reaction, anode materials have to fulfil some basic requirements. Most important properties of the anode are high electron conductivity, sufficient electrocatalytic activity for fuel oxidation reaction, chemical stability, thermal compatibility with other fuel cell components and having sufficient porosity for efficient gas transportation in a high-temperature reducing environment [13]. As one can imagine, it is quite difficult to develop a material that suits all requirements. In this chapter, an overview of currently available anode materials is given including their drawbacks and benefits.

2.1 Ni/YSZ anode materials

At the present time, the most advanced SOFC's are those based on $Ni/Y_2O_3-ZrO_2$ (Ni/YSZ) composite anodes. The Ni in these cermet anodes provides electronic conductivity and catalytic activity, both for direct oxidation and for steam reforming of methane. The YSZ provides both ionic conductivity to allow O^{2-} to diffuse further into the anode and a structural support for the anode that prevents Ni sintering. In some cases, doped ceria is substituted for the YSZ to increase the ionic conductivity.

In addition to exhibiting excellent electrochemical performance in H_2 , Ni cermets are relatively simple to fabricate. For example, tape-calandring and -casting methods have been developed in which the initial green body is a mixture of NiO and YSZ. Because NiO and YSZ do not form solid solutions, even at high temperatures, this green body can be sintered to form a NiO-YSZ composite and then be reduced to form a porous Ni-YSZ cermet. As long as the cermet is approximately 30 vol% Ni, there is sufficient electronic conductivity [14].

Addition of YSZ electrolyte phase into Ni significantly reduces the thermal expansion of the composite material in order to be thermally compatible with the electrolyte. It is generally accepted that the electrochemical activity of Ni anodes for H_2 oxidation reaction depends strongly on the triple phase boundary (TPB). This is the area where fuel gas, Ni and YSZ phases meet (see Figure 3).

There is a significant reduction of electrode polarization resistance of porous Ni electrodes modified by deposition of fine YSZ particles as compared to pure Ni electrodes. This indicates that the YSZ phase in the cermet plays an important electrocatalytic role in the creation of additional reaction sites by extending the two-dimensional reaction zone into three-dimensional reaction zone, significantly enhancing the reaction kinetics in addition to the inhibiting of the coarsening and grain growth of the Ni phase. Therefore the system of composite anode usually consisting of metal-oxide cermet structure has been widely accepted [13].

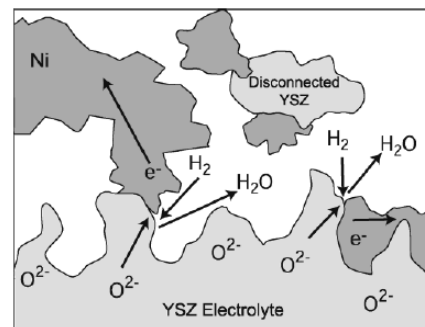


Figure 3: Schematic drawing of triple phase boundaries in Ni/YSZ [14].

However, there are also some drawbacks. The Ni in the cermet tends to agglomerate after prolonged operation, leading to a reduced triple-phase-boundary length and increased resistance.

Besides that, Ni cermets are not well suited for use with hydrocarbon fuels because the high Ni content promotes coking. As nickel is such a good catalyst for hydrocarbon cracking, these cermets can only be utilised in hydrocarbon fuels if excess steam is present to ensure complete fuel reforming, resulting in diluting the fuel and adding to system cost [15]. Also, steam reforming is highly endothermic and when it takes place internally, it creates temperature gradients across the cell, reducing the performance.

Another problem with Ni/YSZ is the known degradation of anode performance upon repeated redox cycling. Such redox cycling may occur occasionally during the long-term operation of larger stacks, and may happen regularly in smaller stacks that must be started and stopped frequently. In the context of a direct hydrocarbon solid oxide fuel cell, the ability to expose the anodes to oxygen, to remove any carbon deposition that may occur periodically, is likely important. The poor redox stability of these cermets may cause cracking during the cycling of the fuel cell. The cermet anode and then the whole stack may be damaged [16].

Low sulphur tolerance of Ni/YSZ anode constitutes another hurdle to the use of natural gas as fuel. The deactivation from sulphur poisoning occurs because H_2S strongly absorbs on active sites of nickel, leading to the substantial reduction in the rate of electrochemical reaction occurring at the triple phase boundaries [17].

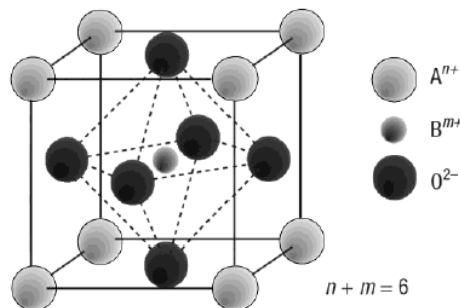
2.2 Cu-CeO₂ anode materials

Cu-ceria cermet anodes work well when the operating temperature is below 800°C. However, the possible sintering of the Cu particles could be a potential problem because of its relatively low melting point (1085°C) during long-term operation at high temperatures.

On the other hand, for some applications such as portable SOFCs or SOFC driven engines, a redox stable anode is required to keep the fuel cell system robust. The volume change of the Cu-CeO₂ anode during redox cycling will cause degradation of the stack. Therefore, this cermet is not quite suitable and redox stable anodes are still in high demand [15].

2.3 Perovskite anode materials

The perovskite oxide formula can be written as ABO_3 where A is a large cation with a coordination number of 12 and B is a small cation with a coordination number of 6 (see Figure 4). These materials can accommodate a large content of oxygen vacancies; therefore some perovskites are good oxygen ionic conductors. The small B-site in the perovskite allows first row transition elements to be introduced in the lattice. These elements exhibit multi-valence under different conditions, which may be the source of high electronic conductivity. Good ionic and mixed conductivity is found in several perovskite oxides [15].

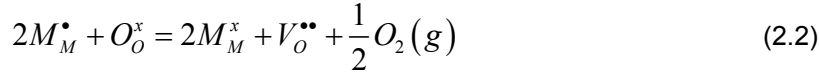


For instance, $(La_{1-x}Sr_x)Cr_{1-y}M_yO_{3-\delta}$ (LSCM) perovskite materials seem to be possible SOFC anode candidates. LSCM materials can be considered as solid solutions of $La_xSr_{1-x}CrO_3$ (LSC) and $La_xSr_{1-x}MnO_3$ (LSM). As a traditional interconnect material, LSC has high stability in an anodic environment. On the other hand, as a common cathode material, LSM has higher conductivity but is not stable in reducing atmosphere [10].

Figure 4: Unit cell of ABO_3 perovskite structure [14].

Tao and Irvine [11] reported the anode performance of complex perovskites based upon Cr and Mn forming compositions of LSCM. Cr^{III} is well known to strongly prefer six-fold coordination. So it is difficult to introduce the oxygen vacancies required for oxide-ion conduction into the $LaCrO_3$ lattice. When the B-sites are doped by other multivalence

transition elements that do tolerate reduced oxygen coordination, such as Mn (or Fe, Co, Ni or Cu) oxygen vacancies may be generated at the B-site dopants in a reducing atmosphere at high temperature. Thus, a significant degree of B-site dopant is required to generate enough oxygen vacancies in order to achieve high oxygen-ion conductivity. The reaction of the oxygen vacancy formation at low pO_2 is given in equation (2.2) in Kröger-Vink notation.



Previous work of others has been focused upon doped lanthanum chromite, where doping is used in the solid state chemical sense of up to 20% dopant on the B-site, usually 5 or 10%. Tao and Irvine reported a complex perovskite where transition metal species occupy the B-site in excess of the percolation limit (e.g. >33%). Such dramatic replacement of an active B-site ion by another element would normally significantly degrade its functionality; however, if the two elements act in a complementary fashion, then an improved new material may be achieved.

Zha et al. [10] have investigated the redox stability of $(La_{0.75}Sr_{0.25})Cr_{1-y}M_yO_3$. They find that the crystal structure changes from hexagonal in air to orthorhombic in H_2 for three LSCM compositions (i.e. $y=0.4$, $y=0.5$ and $y=0.6$). This transformation is accompanied by a low volume change (1%), indicating a good structural stability under redox conditions.

The Thermal Expansion Coefficient (TEC) of LSCM is matching quite well with the TEC of the YSZ electrolyte. Tao and Irvine [18] performed thermal expansion experiments on A-site deficient LSCM $((La_{0.75}Sr_{0.25})_{0.95}Cr_{0.5}M_{0.5}O_3)$ and found a TEC of $8.9 \cdot 10^{-6} K^{-1}$ in the temperature range $64 - 435^\circ C$ and $10.1 \cdot 10^{-6} K^{-1}$ between 520 and $965^\circ C$. For YSZ they measured a TEC of $10.3 \cdot 10^{-6} K^{-1}$. (Note that the yttrium content in YSZ is not given.) Jiang et al. [19] found a TEC of $La_{0.75}Sr_{0.25}Cr_{0.5}M_{0.5}O_3$ sintered at $1200^\circ C$ with a value of $9.2 \cdot 10^{-6} K^{-1}$ in the range of $34 - 135^\circ C$ and $13.7 \cdot 10^{-6} K^{-1}$ between 161 and $900^\circ C$. They also give the value of $10.3 \cdot 10^{-6} K^{-1}$ for YSZ (8 mol% yttrium).

In Figure 5 the total conductivity of LSCM as function of pO_2 and as function of temperature is given [18]. ECN also measured the total conductivity of LSCM and they found an increasing conductivity at increased sinter temperatures and the same effect was found at increased operating temperature. However, the lateral conductivity is not high.

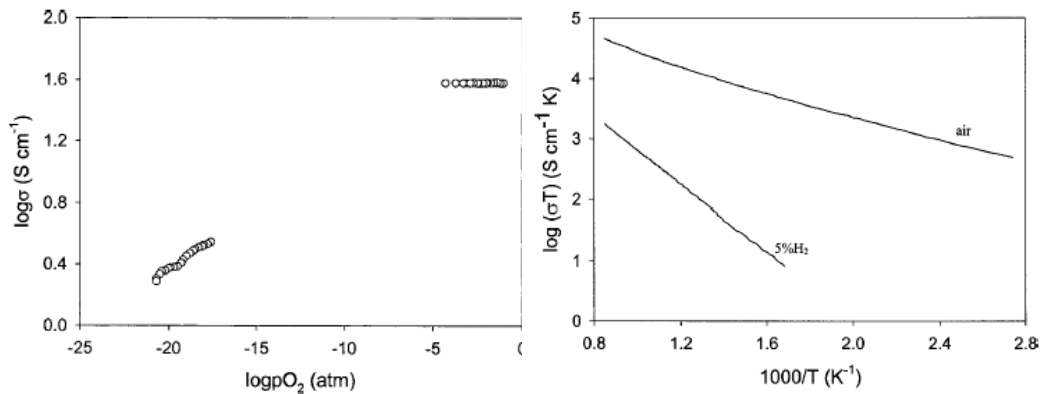


Figure 5: Conductivity measurements on $La_{0.75}Sr_{0.25}Cr_{0.5}Mn_{0.5}O_{3-\delta}$ (left) conductivity vs. pO_2 at $900^\circ C$ (right) conductivity in 5% H_2 and air as function of temperature [18].

2.4 Comparison of other materials

In Table 2 a comparison of different anode materials is given. The Ni/YSZ cermet is extensively discussed above and its drawbacks are mentioned. Cu/YSZ has a better redox stability and is less sensitive to carbon deposition than Ni/YSZ. However, as with the Cu-CeO₂ anodes, the sintering/ agglomeration of Cu particles can be a problem.

Table 2: Comparison of different anode materials for SOFCs [15]

Structure	Typical materials	Stability in reducing atmosphere	Ionic conductivity	Electronic conductivity	Chemical compatibility with YSZ	Thermal compatibility with YSZ	Performance using H ₂ as fuel	Performance using CH ₄ as fuel	Redox stability
Mixture	Ni-YSZ	✓	✓	✓	✓	✓	✓	✗	✗
Mixture	Cu-YSZ	?	✓	✓	✓	✓	✓	✓	✓
Fluorite	YZT, ScYZT CGO	✓	✓	✗	✓	✓	ok	ok	✓
Perovskite	La _{1-x} Sr _x Cr _{1-y} Tm _y O ₃	✓	?	✓	✓	✓	✓	✓	✓
Pyrochlore	Gd ₂ TiMoO ₇	✗	ok	✓	✓	?	?	?	✗
Tungsten bronze	Sr _{0.6} Ti _{0.2} Nb _{0.8} O ₃	✓	✗	✓	✓	?	✗	?	✓
Monoclinic S.G. C2/m	Nb ₂ TiO ₇	✓	✗	✓	✓	✗	?	?	✗

Fluorite structures in general have a too low electronic conductivity to be used as anode material. The rutile structure (not mentioned in Table 2), such as Nb₂TiO₆, is not a good structure either because of a low ionic conduction and its thermal expansion coefficient. The bad ionic conductivity is also visible at tungsten bronze structures, while the pyrochlore structure is not redox stable. A promising material as alternative for the common Ni/YSZ anode is the perovskite structure [15].

2.5 Electrochemical Impedance Spectroscopy

The principal of Electrochemical Impedance Spectroscopy (EIS) is the probing of an electrochemical system with a small AC perturbation, $V_0 \cdot e^{j\omega t}$, over a range of frequencies. The response on this signal is measured. There is a certain phase shift between the ingoing and measured signals, which is a result of the impedance of the system. Like resistance, impedance is a measure of the ability of a circuit to resist the flow of an electrical current [20], [21].

This results in the relation for the impedance (resistance):

$$Z(\omega) = \frac{V(\omega)}{I(\omega)} = \frac{V_0 \cdot e^{j\omega t}}{I_0 \cdot e^{j(\omega t + \varphi)}} = \frac{V_0}{I_0} [\cos \varphi - j \sin \varphi] \quad (2.1)$$

And a relation for the admittance (conductance, inverse of impedance):

$$Y(\omega) = \frac{1}{Z(\omega)} = \frac{I_0 \cdot e^{j(\omega t + \varphi)}}{V_0 \cdot e^{j\omega t}} = \frac{I_0}{V_0} [\cos \varphi + j \sin \varphi] \quad (2.2)$$

These relations consist of a real part plus an imaginary part. These different parts of the relation can be plotted versus each other. The real part can be put on the x-axis and the imaginary part on the y-axis resulting in a typical impedance curve of which each point of this curve represent the signal at a different frequency.

One of the most attractive aspects of impedance spectroscopy as a tool for investigating the electrical and electrochemical properties of materials is the direct connection that often exists between the behaviour of a real material and that of an idealized model circuit consisting of discrete electrical components. It is then possible to compare or fit the impedance data to equivalent elements, which are representative to the physical processes taking place in the material [22]. However, one should be aware of the fact that these processes are not necessarily linked to the equivalent elements on a one-to-one basis.

After measuring the impedance of a sample, data should be checked to see if the system was stable and if the sample was in equilibrium with the environment during the measurement. This check can be performed by using the Kramers-Kronig program for data validation. If the system was in equilibrium, one can start making a fit using the Complex Non-linear Least Squares (CNLS) method by using the equivalent elements given in Table 3 [20].

Table 3: Impedance and admittance of circuit elements

Equivalent element	Description	Admittance	Impedance
R	Resistance	$1/R$	R
C	Capacitance	$j\omega C$	$1/(j\omega C)$
L	Inductance	$1/(j\omega L)$	$j\omega L$
W	Warburg	$Y_0\sqrt{j\omega}$	$Z_0/\sqrt{j\omega}$
Q	CPE	$Y_0(j\omega)^n$	$Z_0/(j\omega)^n$
G	Gerischer	$Y_0\sqrt{k+j\omega}$	$Z_0/\sqrt{k+j\omega}$

Deviations from 'ideal' dispersions, characterised by the above-mentioned equivalent elements, can often be described by the Constant Phase Element (CPE).

$$Y_{CPE} = Y_0 (j\omega)^n = Y_0 \omega^n \left[\cos \frac{n\pi}{2} + j \sin \frac{n\pi}{2} \right] \quad (2.3)$$

The CPE is represented by the equivalent element Q. The CPE is a very general type of dispersion relation and can be brought back to other equivalent elements in the following cases:

- if $n=1$ this equation describes capacitance: $C=Y_0$
- if $n=1/2$ this equation describes Warburg diffusion: $\sigma=Y_0$
- if $n=0$ this equation describes resistance: $R=1/Y_0$
- if $n=-1$ this equation describes inductance: $L=1/Y_0$

These equivalent elements can be put together into a so-called Circuit Description Code (CDC). The CDC presents a unique way to define an equivalent circuit in terms suitable for computer processing. Equivalent elements that are connected in series are put between "square" brackets and equivalent elements that are connected parallel are put between "round" brackets.

2.6 Polarisation

Polarisation is a voltage loss or overpotential voltage, which is a function of current density. In SOFCs three polarisation effects are important i.e. ohmic polarisation, concentration polarisation and activation polarisation. These polarisation effects all contribute in a certain extent to the impedance of the SOFC materials and can therefore be found in electrochemical impedance spectroscopy measurements.

Ohmic polarisation or ohmic loss is the resistance to the motion of electrical charges in the material. For instance, the motion of oxygen ions is influenced by the ionic resistivity of the electrolyte and the motion of electrons or electron holes is influenced by the electronic resistivity of the electrodes. However, in SOFCs, the main contribution to the ohmic polarisation is usually from the electrolyte. The ionic resistivity of YSZ is much bigger than the electronic resistivities of the cathode and anode.

The physical resistance to the transport of gaseous species through the material at a given current density generates a polarisation loss. This principle is called concentration polarisation. Concentration polarisation depends on the porosity, tortuosity and thickness of

the anode and, to a lesser extent, Knudsen diffusion, adsorption/ desorption and surface diffusion phenomena. In electrochemical impedance measurements, the concentration polarisation can be analysed by using the Warburg element for diffusion (see also 2.5 *Electrochemical Impedance Spectroscopy*). In this research, concentration polarisation effects are expected to be relatively low because of the usage of hydrogen as fuel. Hydrogen is a small molecule and has a low molecular weight and will therefore have fast diffusion and experience less resistance.

Electrode reactions involve charge transfer as a fundamental step, wherein a neutral species is converted into an ion and the other way around. This charge transfer is, together with adsorption/ desorption during electrode reactions, representing the third polarisation phenomenon called activation polarisation [5].

3 Experimental

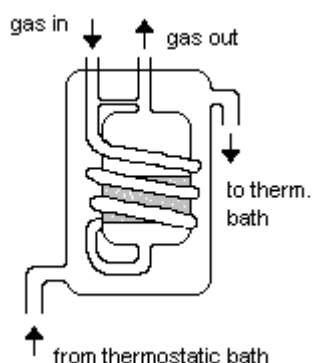
In this chapter the set-up for the electrochemical impedance spectroscopy measurements as well as the samples and measurement procedure will be discussed.

3.1 The set-up

Hydrogen and nitrogen are entering the set-up through a mass flow controller (Brooks MFC 5850E). These mass flow controllers are operated by a control unit (Brooks instruments 5898). With the mixing of these gases, a certain wanted p_{H_2} can be established.

After blending of the gases, the gas mixture flows past a protection tube. If the gasflow through the set-up is blocked, the gas escapes the set-up through this overpressure protection tube.

The gas flows through two water bubblers to enrich the gasflow with water. A schematic drawing of one of these water bubblers can be seen in Figure 6. The temperature of the water bubblers can be controlled with two thermostatic baths. The purpose of these thermostatic baths is to control the humidity of the gasflow. Two thermostatic baths in series makes it possible to over-saturate the gas flow with water by putting the first thermostatic bath (Labovisco T1000) 5 °C higher then the second thermostatic bath (Julabo F25). The second thermostatic bath is put on the wanted temperature. By this way the p_{H_2O} can be set very accurate.



After the gas passes the first water bubbler, the temperature of the water-enriched gas should be kept above the temperature of the bubblers through the rest of the set-up to prevent condensation of water in the tubes. The tubes are heated and isolated and the temperature is controlled with the presence of four thermocouples (Eurotherm 91E) namely:

- between the two bubblers
- at the inlet of the quartz tube with the sample holder
- in the quartz tube itself, close to the sample
- at the outlet of the quartz tube

Figure 6: Schematic drawing of one of the water bubblers used in the set-up

How the sample holder is situated in the quartz tube in the furnace is discussed in paragraph 3.2 *Close-up of the sample holder*. The furnace is equipped with a temperature controller (Eurotherm 91E).

For impedance measurements a frequency response analyser (Schlumberger HF FRA SI 1260) is used in combination with an electrochemical interface (Solartron SI 1287). The whole set-up is connected with and operated from a computer with the program *Zplot for Windows*.

3.2 Close-up of the sample holder

In Figure 7a, the quartz tube is presented schematically. In its whole, this quartz tube is situated inside a furnace with a maximum temperature of approximately 900 °C. Inside the quartz tube, a ceramic tube is protecting the wiring and thermocouple that are leading to the sample holder in the upper part of the quartz tube.

The sample holder itself, which is displayed in Figure 7b, consists of a round ceramic holder with an inside diameter that is about the same as the diameter of the sample. The sample is enclosed by two platinum meshes that serve as current collectors. Each platinum mesh is connected with two platinum wires to create the electric circuit with the electrochemical measurement set-up. The sample and the current collectors are, on their turn, placed

between two porous ceramic disks to optimise the gas flow to the sample. On top of this configuration, a weight is put to increase contact between the platinum meshes and the sample. The lateral conductivity of the electrode material is assumed to be good enough to lead the current in the lateral direction of the material. This is important because the platinum meshes will only make contact with the electrode material on a restricted amount of points.

A thermocouple is placed at the bottom of the sample holder to measure the temperature as close to the sample as possible.

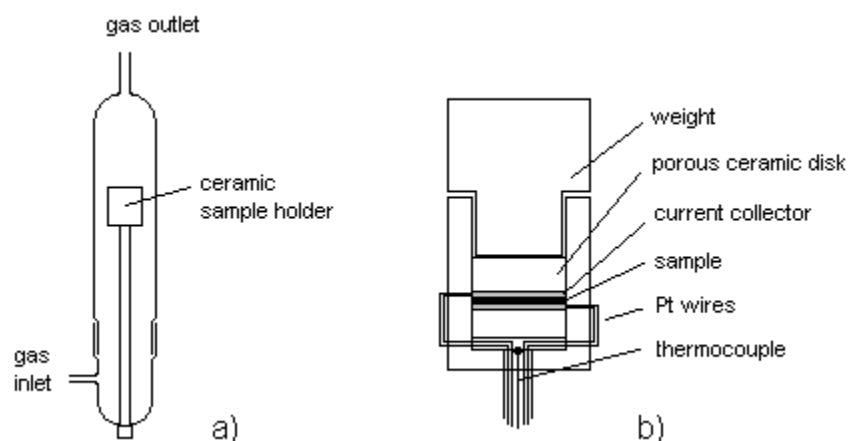


Figure 7: Schematic drawing of a) the quartz tube with the ceramic sample holder b) the ceramic sample holder enlarged.

3.3 Sample geometry and composition

The samples that are discussed in this research are symmetric cells. This means that the same anode material is deposited on both sides of the electrolyte (see Figure 8). The advantage of such a configuration is that there is no need for a reference electrode to distinguish both electrodes. For this reason also the electrolyte material can be remained very thin and influences of the electrolyte on the impedance data are therefore minimised. This is because ohmic losses are mainly caused by the electrolyte (see paragraph 2.6 *Polarisation*) and this effect will now be smaller. For fundamental research on the anode material it is also desirable to exclude other materials from the set-up.

The symmetric cells are produced and supplied by Energy research Centre of the Netherlands (ECN). The cells are all composed of a certain configuration of strontium doped lanthanum chromite-manganites (LSCM) on a 3 mol% yttria-stabilised tetragonal zirconia (TZ3Y) electrolyte. The LSCM material has the perovskite structure and is doped with strontium on the A-site and with manganese on the B-site. It is possible for the A-site as well as the B-site in the perovskite material to be somewhat depleted without disrupting the crystal structure.

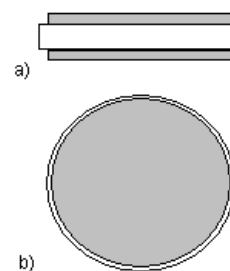


Figure 8: Cell configuration from a) the side b) the top. The grey parts represent the anode material and the white parts the electrolyte.

The anode material typically has a thickness of 40 μm and is applied on the YSZ electrolyte by screen-printing on both sides. The electrolyte has a thickness of approximately 130 μm . The diameter of the symmetric cell (= diameter of the electrolyte layer) is 2.5 mm. The electrode surface area differs per sample.

ECN supplied samples with configurations of LSCM varied by the applied sinter temperature and sintering environment (air or hydrogen) during sample preparation. Following samples are measured:

- two samples with anode layers of $\text{La}_{0.75}\text{Sr}_{0.25}\text{Cr}_{0.5}\text{Mn}_{0.5}\text{O}_3$ sintered at $1200\text{ }^\circ\text{C}$ in air
- two samples with anode layers of $\text{La}_{0.75}\text{Sr}_{0.25}\text{Cr}_{0.5}\text{Mn}_{0.5}\text{O}_3$ sintered at $1500\text{ }^\circ\text{C}$ in air.
- one sample with anode layers of $\text{La}_{0.75}\text{Sr}_{0.25}\text{Cr}_{0.5}\text{Mn}_{0.5}\text{O}_3$ sintered at $1200\text{ }^\circ\text{C}$ in hydrogen.
- two samples with anode layers of $\text{La}_{0.75}\text{Sr}_{0.25}\text{Cr}_{0.5}\text{Mn}_{0.5}\text{O}_3$ sintered at $1200\text{ }^\circ\text{C}$ in air, on which gold current collectors are applied.

3.4 Measuring procedure

The measuring procedure is equal for all samples. First, measurements are performed at a temperature around $850\text{ }^\circ\text{C}$. Then the temperature is step-wise lowered to around $650\text{ }^\circ\text{C}$ to see the temperature influence. Finally the sample is measured again at this lower temperature. During the measurements the total gas flow is kept constant at $100\text{ ml}\cdot\text{min}^{-1}$. When less hydrogen is needed, more nitrogen is added to the gas feed to maintain this constant flow.

More specific, each sample is measured by following these steps:

1. Impedance measurements at a p_{H_2} range of $1.98\cdot 10^4 - 9.9\cdot 10^4$ Pa with a fixed $p_{\text{H}_2\text{O}}$ of $2.34\cdot 10^3$ Pa at a temperature around $850\text{ }^\circ\text{C}$.
2. Impedance measurements at a $p_{\text{H}_2\text{O}}$ range of $1.99\cdot 10^4 - 1.23\cdot 10^3$ Pa with a fixed p_{H_2} of $8.14\cdot 10^4$ Pa at a temperature around $850\text{ }^\circ\text{C}$.
3. Impedance measurements under standard conditions ($p_{\text{H}_2} = 9.90\cdot 10^4$ Pa and $p_{\text{H}_2\text{O}} = 2.34\cdot 10^3$ Pa) at temperatures ranging from $850 - 650\text{ }^\circ\text{C}$ in steps of $-50\text{ }^\circ\text{C}$.
4. Impedance measurements at a p_{H_2} range of $1.98\cdot 10^4 - 9.9\cdot 10^4$ Pa with a fixed $p_{\text{H}_2\text{O}}$ of $2.34\cdot 10^3$ Pa at a temperature around $650\text{ }^\circ\text{C}$.
5. Impedance measurements at a $p_{\text{H}_2\text{O}}$ range of $1.99\cdot 10^4 - 1.23\cdot 10^3$ Pa with a fixed p_{H_2} of $8.14\cdot 10^4$ Pa at a temperature around $650\text{ }^\circ\text{C}$.

These measurements are done at open circuit voltage (OCV) with a frequency range of 10 kHz to 10 mHz with an amplitude of 10 mV. Subsequently all data is verified with the *Kramers-Kronig* validation software for impedance spectroscopy measurements.

4 Results and discussion

ECN supplied samples with configurations of LSCM varied by the applied sinter temperature and sintering environment (air or hydrogen) during sample preparation. The goal of this research is to determine the influence of these parameters on the electrochemical properties of the anode material. In this chapter the experimental data of the different samples is presented.

The following samples are measured:

- two samples with anode layers of $\text{La}_{0.75}\text{Sr}_{0.25}\text{Cr}_{0.5}\text{Mn}_{0.5}\text{O}_3$ sintered at $1200\text{ }^\circ\text{C}$ in air.
- two samples with anode layers of $\text{La}_{0.75}\text{Sr}_{0.25}\text{Cr}_{0.5}\text{Mn}_{0.5}\text{O}_3$ sintered at $1500\text{ }^\circ\text{C}$ in air.
- one sample with anode layers of $\text{La}_{0.75}\text{Sr}_{0.25}\text{Cr}_{0.5}\text{Mn}_{0.5}\text{O}_3$ sintered at $1200\text{ }^\circ\text{C}$ in hydrogen.
- two samples with anode layers of $\text{La}_{0.75}\text{Sr}_{0.25}\text{Cr}_{0.5}\text{Mn}_{0.5}\text{O}_3$ sintered at $1200\text{ }^\circ\text{C}$ in air, on which gold current collectors are applied (one by sputtering and one by painting a gold paste).

The total impedance of a symmetric cell consists of the resistance of the electrolyte (R_{el}) plus two times the electrode polarisation ($2 R_{pol}$). R_{el} is actually the ohmic resistance of the total cell (electrolyte and electrodes) but the influence of the electrodes on the ohmic resistance is negligible. The ionic resistivity of YSZ is much bigger than the electronic resistivities of the electrodes.

R_{pol} is coupled with a factor two because there is an electrode layer that contributes to the polarisation on both sides of the electrolyte. An example of an impedance measurement is given (Figure 9) to illustrate the position of R_{el} and R_{pol} in an impedance plot. However, this image shows raw data of one measurement with both axes given in Ohm. Calculations are needed to find the values of R_{el} and R_{pol} in $\text{Ohm}\cdot\text{cm}$ and $\text{Ohm}\cdot\text{cm}^2$ respectively. In literature, the R_{pol} in $\text{Ohm}\cdot\text{cm}^2$ is often referred to as the Area Specific Resistance (ASR) of the measured cell.

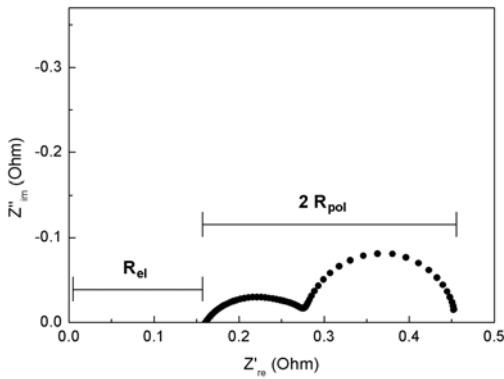


Figure 9: Example of an impedance measurement to illustrate the position of R_{el} and R_{pol} in an impedance plot. (LSCM sintered at $1200\text{ }^\circ\text{C}$ gold-paint covered, $p_{H_2O} = 2.34 \cdot 10^3\text{ Pa}$, $p_{H_2} = 9.90 \cdot 10^4\text{ Pa}$, $T = 850\text{ }^\circ\text{C}$)

The p_{O_2} values that are used in this chapter are calculated from the hydrogen and water partial pressures and the equilibrium constant of the water formation reaction formula (equation 4.1).

$$p_{O_2} = \left(\frac{p_{H_2O}}{p_{H_2} \cdot K_{eq}} \right)^2 \quad (4.1)$$

Furthermore the operating temperatures, under which the samples are measured, usually differ some degrees from the wanted value (for instance $848\text{ }^\circ\text{C}$ instead of $850\text{ }^\circ\text{C}$). This small difference is caused because of the fact that the operating temperature is measured with a

thermocouple close to the sample while the set-point of the furnace is higher. The set-point of the furnace has to be estimated to establish the right temperature close to the sample resulting sometimes in a small discrepancy.

4.1 $\text{La}_{0.75}\text{Sr}_{0.25}\text{Cr}_{0.5}\text{Mn}_{0.5}\text{O}_{3-\delta}$ sintered at $1200\text{ }^{\circ}\text{C}$ in air

Two kinds of these samples, sintered at $1200\text{ }^{\circ}\text{C}$ in air, are supplied by ECN. These samples are produced by using the same production parameters, but they are produced in different batches. The two samples only differ in functional anode surface area. The first batch has an anode surface area of 3.8 cm^2 and the second batch has an anode surface area of 4.4 cm^2 . Figure 10 shows SEM images taken by ECN of $\text{La}_{0.75}\text{Sr}_{0.25}\text{Cr}_{0.50}\text{Mn}_{0.50}\text{O}_{3-\delta}$ sintered at $1200\text{ }^{\circ}\text{C}$ in air. This LSCM has a porosity of 27% and an average particle size of $0.7\text{ }\mu\text{m}$.

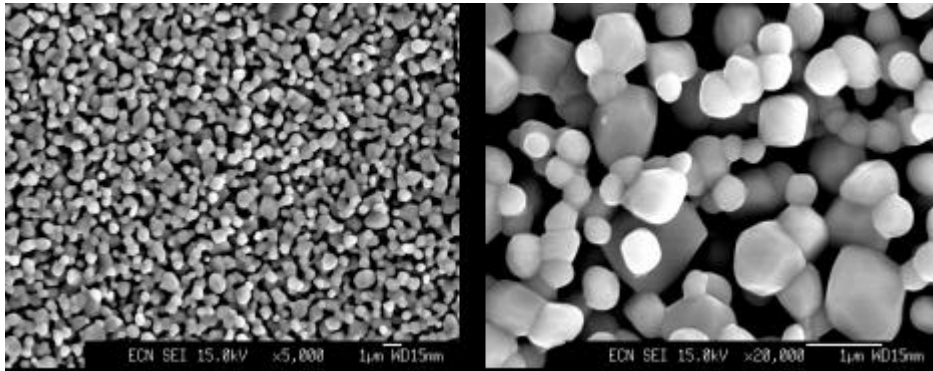


Figure 10: SEM images taken by ECN of LSCM sintered at $1200\text{ }^{\circ}\text{C}$ in air. Left) $\times 5,000$ right) $\times 20,000$.

Impedance spectroscopy data of the sample from the first batch

The measurements are performed according to the measurement procedure given in Chapter 3. The first measurement of the measuring procedure is at fixed water partial pressure at varying hydrogen partial pressures at a temperature of $840\text{ }^{\circ}\text{C}$. The result of this measurement is given as example in Figure 11. After verifying this data with the *Kramers-Kronig* software, the data is loaded in the program called *Equivalent circuit for Windows*. With this program equivalent circuit models are found that fit the data. The result of the fitting of this first measurement, together with the fitting of all other measurements concerning this sample, is given in Appendix 1.

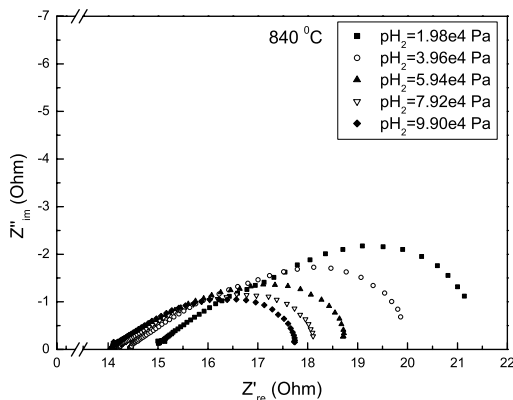


Figure 11: Example of impedance measurement at $840\text{ }^{\circ}\text{C}$, $p_{\text{H}_2\text{O}}=2.34 \cdot 10^3\text{ Pa}$.

The measurements as a function of p_{H_2} at $840\text{ }^{\circ}\text{C}$ can be properly modelled with the equivalent circuit $R_{\text{el}}(R_1Q_1)(R_2Q_2)(R_3Q_3)$ (see Figure 12) (with exception of the measurement at a p_{O_2} of $9.79 \cdot 10^{-15}\text{ Pa}$). The electrolyte resistance R_{el} is independent of p_{O_2} and has a value of $4.2 \cdot 10^3\text{ Ohm}\cdot\text{cm}$, ($2.4 \cdot 10^{-4}\text{ S}\cdot\text{cm}^{-1}$). In literature [23]-[26], conductivity values for TZ3Y

at 850 °C are in the range of $1.8 \cdot 10^{-2} - 3.0 \cdot 10^{-2} \text{ S} \cdot \text{cm}^{-1}$. The three parallel combinations of a resistance and a CPE in series describe the electrode response. The first CPE shows a Warburg diffusion process with n very close to 0.5. The n -value resulting from the second CPE is in the order of 0.7-0.8 and the third n -value is equal to 1.0, which implies capacitive behaviour. The third CPE, belonging to R_3Q_3 in the equivalent circuit, is visible in the low frequency range. This CPE has a very high capacitance of $\sim 1 \text{ F}$. Such high capacitances can be caused by adsorption of species on the anode surface, in this case hydrogen or water. R_3 has a clear dependency on the hydrogen partial pressure on a log/log scale (slope=-0.44). Besides that, the capacitive behaviour of R_3Q_3 is not present at the measurements as a function of $p_{\text{H}_2\text{O}}$ (as discussed further on) and therefore R_3 is independent of the water partial pressure. So it seems like the capacitive behaviour in the low frequency range is caused by hydrogen adsorption. It is hard to find values of activation energies in literature about hydrogen adsorption on LSCM, but dissociative chemisorption of hydrogen on a nickel surface is about $90 - 100 \text{ kJ} \cdot \text{mol}^{-1}$ [27], [28]. In this case, the activation energy of R_3 at low frequencies is $83 \text{ kJ} \cdot \text{mol}^{-1}$. It is difficult to compare these values, but they do are in the same order of magnitude so hydrogen adsorption is still very likely.

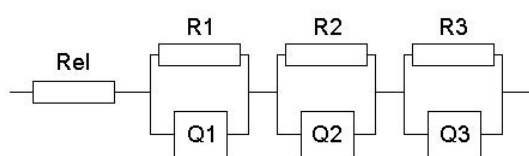


Figure 12: Equivalent circuit for the measurement at 840 °C as a function of p_{H_2}

The measurements as a function of $p_{\text{H}_2\text{O}}$ at 840 °C can be modelled with the equivalent circuit $R_{\text{el}}(R_1Q_1)(R_2Q_2)$. The electrolyte resistance R_{el} has a value of $3.5 \cdot 10^3 \text{ Ohm} \cdot \text{cm}$, ($2.8 \cdot 10^{-4} \text{ S} \cdot \text{cm}^{-1}$) and is again independent of p_{O_2} . In literature [23]-[26], conductivity values for TZ3Y at 850 °C are in the range of $1.8 \cdot 10^{-2} - 3.0 \cdot 10^{-2} \text{ S} \cdot \text{cm}^{-1}$. The first CPE element is representing Warburg diffusion with an n -value of around 0.5 and the second CPE has an n -value in the order of 0.7 – 0.9.

At 650 °C, the electrochemical impedance spectroscopy data can be modelled with the circuit $R_{\text{el}}(R_1Q_1)(R_2Q_2)(R_3Q_3)(R_4Q_4)$. This model nicely fits the data for the measurements as a function of p_{H_2} as well as the measurements as function of $p_{\text{H}_2\text{O}}$. The electrolyte resistance R_{el} is independent of p_{O_2} and has a value of $3.0 \cdot 10^4 \text{ Ohm} \cdot \text{cm}$, ($3.3 \cdot 10^{-5} \text{ S} \cdot \text{cm}^{-1}$) and $3.5 \cdot 10^4 \text{ Ohm} \cdot \text{cm}$, ($2.9 \cdot 10^{-5} \text{ S} \cdot \text{cm}^{-1}$) for the measurements as a function of p_{H_2} and $p_{\text{H}_2\text{O}}$ respectively. In literature [23]-[26], conductivity values for TZ3Y at 650 °C are in the range of $1.7 \cdot 10^{-3} - 5.1 \cdot 10^{-3} \text{ S} \cdot \text{cm}^{-1}$. The values of all other equivalent circuit elements of both measurement series are in good agreement with each other. The first CPE value has an n -value of around 0.5 and therefore implies Warburg diffusion. The second CPE value has an n -value in the range of 0.7-0.8. The third CPE has an n -value slightly higher than 0.5 and the fourth n -value is in the range of 0.9-1.0 and can therefore be attributed to capacitance behaviour. This fourth CPE is resulting from the low frequency range and has a capacity of about 200 – 400 mF. This is quite a large capacity. Capacitances of this order of magnitude can possibly be related to concentration polarisation of the gas phase in the anode material but adsorption is again also possible.

The activation energy of the electrolyte resistance is $69 \text{ kJ} \cdot \text{mol}^{-1}$ as can be seen in Figure 13. Activation energies of TZ3Y in literature [23]-[26] are in the range of $77 - 83 \pm 3 \text{ kJ} \cdot \text{mol}^{-1}$. The total electrode resistance has an activation energy of $185 \text{ kJ} \cdot \text{mol}^{-1}$.

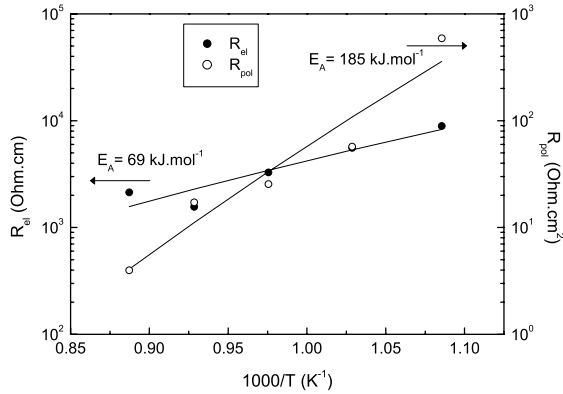


Figure 13: Activation energies of R_{el} and R_{pol} of LSCM sintered at $1200\text{ }^{\circ}\text{C}$ in air (first batch)

In Figure 14, the $p\text{O}_2$ dependencies of the electrolyte resistivity and the electrode polarisation at $650\text{ }^{\circ}\text{C}$ and $840\text{ }^{\circ}\text{C}$ are displayed. There is hardly any dependency in the electrolyte resistance. Slopes vary between -0.06 and $+0.02$ on a log/log scale. The only notable $p\text{O}_2$ -dependency can be found at the electrode polarisation at $840\text{ }^{\circ}\text{C}$ at varied partial hydrogen pressure with a slope of $+0.21$. The electrode polarisation of this measurement is in the range of $7 - 14\text{ Ohm}\cdot\text{cm}^2$.

The sample has an electrode polarisation of around $6\text{ Ohm}\cdot\text{cm}^2$ at the measurement at $840\text{ }^{\circ}\text{C}$ as a function of $p\text{H}_2\text{O}$. And for the measurements at $650\text{ }^{\circ}\text{C}$, this sample has an electrode polarisation of about $500\text{ Ohm}\cdot\text{cm}^2$.

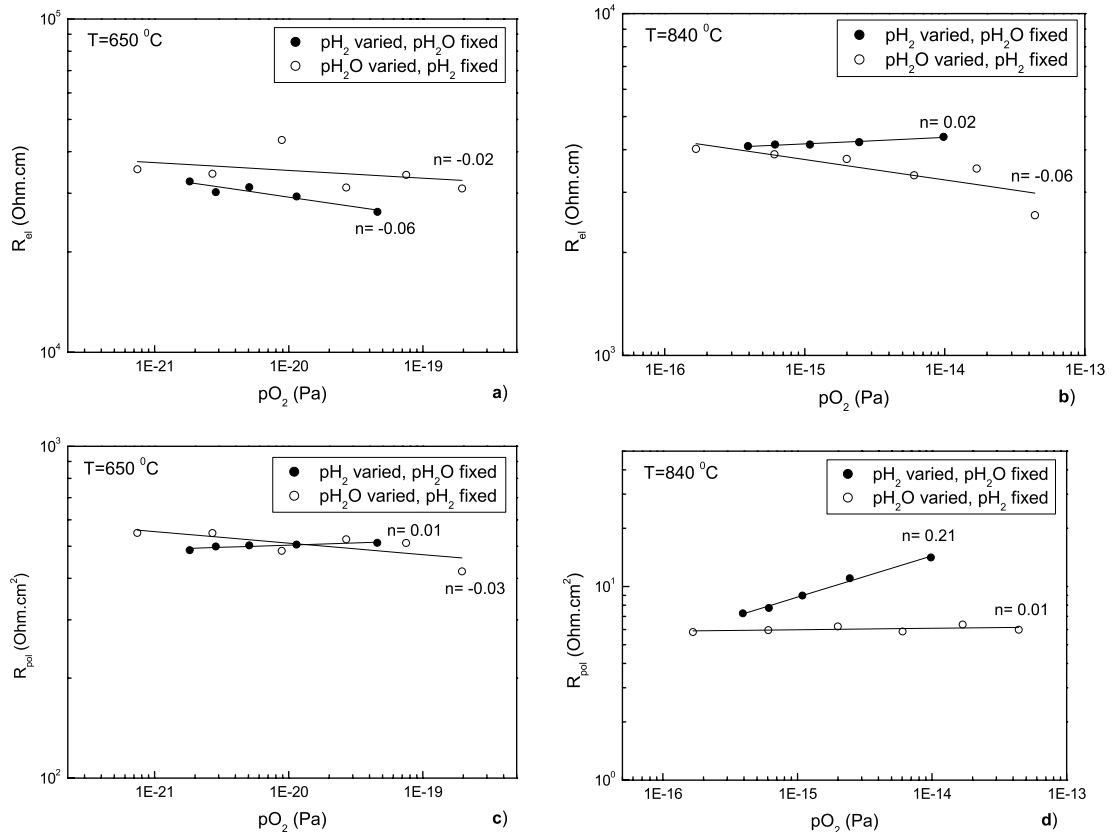


Figure 14: $p\text{O}_2$ dependencies of a) R_{el} at $650\text{ }^{\circ}\text{C}$ b) R_{el} at $840\text{ }^{\circ}\text{C}$ c) R_{pol} at $650\text{ }^{\circ}\text{C}$ d) R_{pol} at $840\text{ }^{\circ}\text{C}$ of LSCM sintered at $1200\text{ }^{\circ}\text{C}$ in air (first batch).

The electrode polarisation at 650 °C is half determined by R_3 (at measurements as function of p_{H_2} as well as p_{H_2O}), having a value of about 250 $\text{Ohm}\cdot\text{cm}^2$. So the process that is fit by R_3Q_3 is dominant at this temperature. As said, the n-value that belongs to the third CPE at 650 °C has a value close to 0.5. The process that causes the highest electrode resistance is therefore probably a diffusion process.

At 840 °C there is no process dominating explicitly. All R-values of the parallel RQ combinations have about an equal contribution to the electrode polarisation.

Impedance spectroscopy data of the sample from the second batch

The fitting data of the impedance measurements of this sample can be found in Appendix 2.

The first measurements at 848 °C as a function of p_{H_2} can be well modelled with the equivalent circuit $R_{el}(R_1Q_1)(R_2Q_2)$. Chi-squared values of the fitting curve are in the order of 10^{-8} . The first CPE is showing Warburg diffusion with an n-value of 0.5 and the second CPE shows capacitor behaviour with an n-value of 0.9 – 1.0. The electrolyte resistance R_{el} is independent of p_{O_2} and has a value of $3.3\cdot 10^3 \text{ Ohm}\cdot\text{cm}$, ($3.0\cdot 10^{-4} \text{ S}\cdot\text{cm}^{-1}$).

The measurements at 848 °C as a function of p_{H_2O} are modelled with one (RQ) combination extra i.e. $R_{el}(R_1Q_1)(R_2Q_2)(R_3Q_3)$. The CPE's have n-values of 0.5, 0.6 and 0.9 – 1.0 respectively. So Warburg diffusion and capacitor behaviour are observed again. The electrolyte resistance R_{el} is independent of p_{O_2} and has a value of $2.8\cdot 10^3 \text{ Ohm}\cdot\text{cm}$, ($3.5\cdot 10^{-4} \text{ S}\cdot\text{cm}^{-1}$). In literature [23]-[26], conductivity values for TZ3Y at 850 °C are in the range of $1.8\cdot 10^{-2} - 3.0\cdot 10^{-2} \text{ S}\cdot\text{cm}^{-1}$. The CPE with the n-value of 0.9 – 1.0 is seen in both equivalent circuits and is probably the same process. This capacitance has a value of 1 – 4 F, which is very high. Such high capacitances can be attributed to adsorption. The involved R-value is quite strongly dependent on the hydrogen partial pressure and less dependent on the water partial pressure. The possible mechanism that belongs to this capacitive behaviour is probably hydrogen adsorption on the anode material.

At 649 °C the data, as a function of p_{H_2} , can be modelled with the equivalent circuit $R_{el}(R_1Q_1)(R_2Q_2)(R_3Q_3)$. The R_{el} has a value of $1.2\cdot 10^4 \text{ Ohm}\cdot\text{cm}$, ($8.1\cdot 10^{-5} \text{ S}\cdot\text{cm}^{-1}$). The n-values corresponding to the CPE values are 0.6 – 0.8, 0.6 – 0.7 and 0.5 – 0.7. There is some spreading in the n-values and no specific behaviour is visible.

The measurements as a function of p_{H_2O} at 642 °C are comparable with the measurements as a function of p_{H_2} . The data can as well be modelled with the equivalent circuit $R_{el}(R_1Q_1)(R_2Q_2)(R_3Q_3)$ and also no specific behaviour can be attributed to the n-values corresponding to the CPE's. The n-values are 0.7 – 0.8, 0.6 – 0.7 and 0.6 – 0.7 respectively. The R_{el} has a value of $1.1\cdot 10^4 \text{ Ohm}\cdot\text{cm}$, ($8.8\cdot 10^{-5} \text{ S}\cdot\text{cm}^{-1}$). In literature [23]-[26], conductivity values for TZ3Y at 650 °C are in the range of $1.7\cdot 10^{-3} - 5.1\cdot 10^{-3} \text{ S}\cdot\text{cm}^{-1}$.

The activation energy of the electrolyte resistance is $65 \text{ kJ}\cdot\text{mol}^{-1}$ as can be seen in Figure 15. Activation energies of TZ3Y in literature [23]-[26] are in the range of $77 - 83 \pm 3 \text{ kJ}\cdot\text{mol}^{-1}$. The total electrode resistance has an activation energy of $147 \text{ kJ}\cdot\text{mol}^{-1}$.

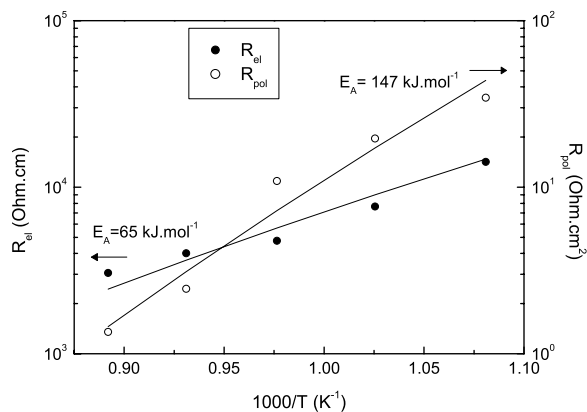


Figure 15: Activation energies of R_{el} and R_{pol} of LSCM sintered at 1200 °C in air (second batch)

In Figure 16, the pO_2 dependencies of the electrolyte resistivity and the electrode polarisation at 649 °C and 848 °C are displayed. As with the sample of the first batch, the only notable pO_2 -dependency can be found at the electrode polarisation at 840 °C at varied partial hydrogen pressure, this time with a slope of +0.25. The electrode polarisation of this measurement is in the range of 1 – 3 Ohm·cm².

The sample has an electrode polarisation of around 1.3 Ohm·cm² at the measurement at 848 °C as a function of pH_2O . And for the measurements at 649 °C, this sample has an electrode polarisation of about 50 Ohm·cm².

Comparable to the sample from the first batch, the R_3 is contributing the most to the electrode polarisation at 649 °C for both types of measurements (as function of pH_2 and pH_2O). The n -values are a bit higher than 0.5 so it cannot clearly be said that this process is diffusion. But when compared with these results from the sample of the first batch, diffusion is very likely. Again, at 848 °C there is no process dominating explicitly. All R -values of the parallel RQ combinations have about an equal contribution to the electrode polarisation.

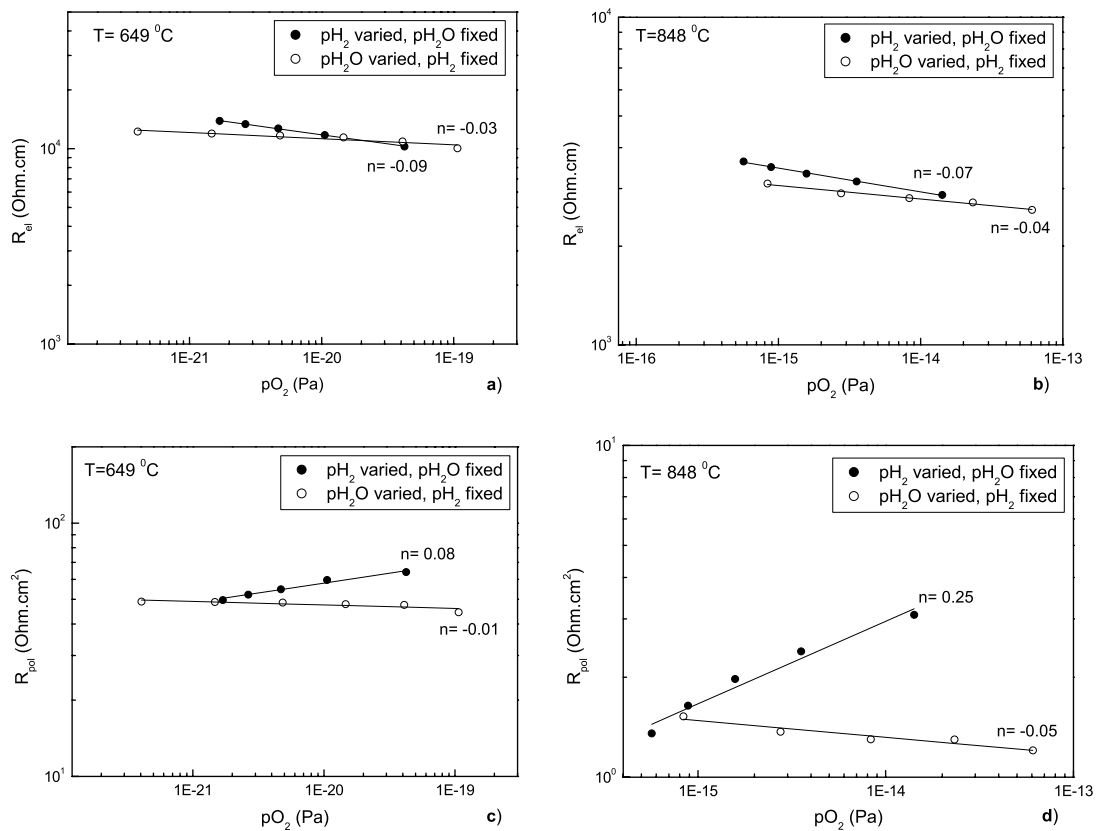


Figure 16: pO_2 dependencies of a) R_{el} at 649 °C b) R_{el} at 848 °C c) R_{pol} at 649 °C d) R_{pol} at 848 °C of LSCM sintered at 1200 °C in air (second batch).

Discussion

The measured electrolyte resistances of the first batch are somewhat bigger than the electrolyte resistances of the second batch. It is hard to say what is exactly causing this difference. It is possible that both samples unintentionally do differ in microstructure or that the chemical composition differs to some extent. But what is more important is that both electrolyte resistances differ a factor 50 to 100 with the values given in literature [23]-[26] (see Table 4).

Table 4: Results on electrolyte conductivity and activation energies of R_{el} and R_{pol}

	1 st batch	2 nd batch	Literature
σR_{el} at 650 °C (at varying pH_2) ($S \cdot cm^{-1}$)	$3.3 \cdot 10^{-5}$	$8.1 \cdot 10^{-5}$	$1.7 \cdot 10^{-3} - 5.1 \cdot 10^{-3}$
σR_{el} at 650 °C (at varying pH_2O) ($S \cdot cm^{-1}$)	$2.9 \cdot 10^{-5}$	$8.8 \cdot 10^{-5}$	
σR_{el} at 850 °C (at varying pH_2) ($S \cdot cm^{-1}$)	$2.4 \cdot 10^{-4}$	$3.0 \cdot 10^{-4}$	$1.8 \cdot 10^{-2} - 3.0 \cdot 10^{-2}$
σR_{el} at 850 °C (at varying pH_2O) ($S \cdot cm^{-1}$)	$2.8 \cdot 10^{-4}$	$3.5 \cdot 10^{-4}$	
$E_A R_{el}$ ($kJ \cdot mol^{-1}$)	69	65	$77 - 83 \pm 3$
$E_A R_{pol}$ ($kJ \cdot mol^{-1}$)	185	147	-

The most likely explanation for the difference in the electrolyte resistances with literature values is that the measured electrolyte resistance is increased by other resistances, coming from the electrode material (resistances from, for instance, contacting problems).

If the contact between the LSCM grains has not been optimal, this would lead to bad conducting properties of the electrode, which will influence the measured value of the electrolyte resistance. To get more insight on this possibility, measurements on LSCM will be done at higher sinter temperatures of the LSCM material. A higher sinter temperature will lead to better inter-granular contact (see paragraph 4.2).

Another possibility (which is more likely, regarding the order of magnitude of the electrolyte resistance) is the existence of a spreading resistance in the electrode material coming from contacting problems between the platinum meshes and the electrode material. This will be discussed later on in paragraph 4.4.

There is a difference in activation energy for the electrode polarisation between the two samples. This difference is quite significant. Both activation energies are high and such high activation energies can often be attributed to gas transport limitation processes. Also at 650 °C a big contribution of R_3 on the electrode polarisation is found. This resistance, with a corresponding CPE with $n \sim 0.5$, contributes to the possibility of a diffusion process.

At around 850 °C there is a process in the low frequency range, contributing to the electrode polarisation, which most likely is adsorption of hydrogen to the anode material.

The electrode resistance is mostly dependent of pO_2 for the measurements at 850 °C as a function of pH_2 . This is valid for both samples. There also is a very small dependency at 650 °C as a function of pH_2 . Therefore, it is very likely that surface processes mainly determine the electrode polarisation (gas transport limitation/ adsorption of hydrogen gas) instead of bulk processes.

The electrode polarisation is also higher when compared to literature. The electrode polarisation at around 850 °C is between $1.2 \text{ Ohm} \cdot \text{cm}^2$ and $14.1 \text{ Ohm} \cdot \text{cm}^2$ for different wet H_2/N_2 gas compositions. Tao and Irvine [11],[18] report an electrode polarisation of $La_{0.75}Sr_{0.25}Cr_{0.5}Mn_{0.5}O_{3-\delta}$ of $0.9 \text{ Ohm} \cdot \text{cm}^2$ in wet 5% H_2/Ar at 925 °C and an electrode polarisation of $0.47 \text{ Ohm} \cdot \text{cm}^2$ in wet H_2 at 925 °C. The sinter temperature they used during LSCM preparation is not clear and the operation temperature is higher, but the difference in electrode polarisation is still too large. As said, probably contacting problems are causing these higher resistances.

4.2 $La_{0.75}Sr_{0.25}Cr_{0.5}Mn_{0.5}O_{3-\delta}$ sintered at 1500 °C in air

It is possible that, due to an enhanced contact between the LSCM grains at higher sinter temperatures, better conducting properties are obtained. The enhanced contact is coming from more extensive necking of the grains. Figure 17 shows SEM images taken by ECN of $La_{0.75}Sr_{0.25}Cr_{0.50}Mn_{0.50}O_{3-\delta}$ sintered at 1450 °C in air. This LSCM has a porosity of 23% and an average particle size of $1.7 \mu\text{m}$. The necking and subsequent increased grain size can be seen when Figure 17 is compared with Figure 10.

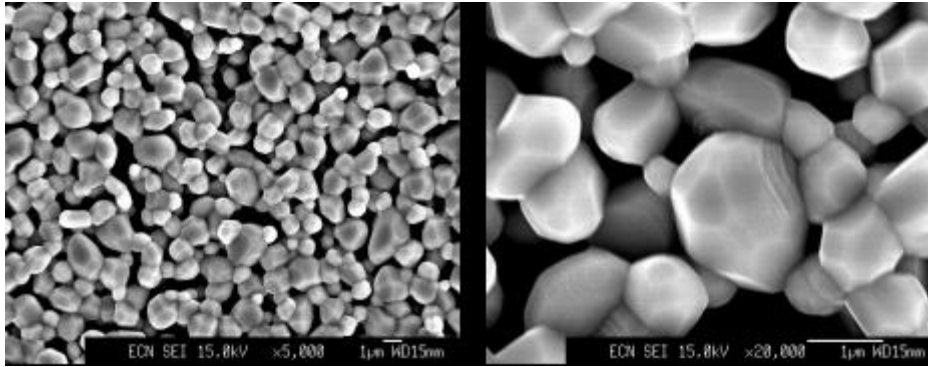


Figure 17: SEM images taken by ECN of LSCM sintered at 1450 °C in air. Left) x5,000 right) x20,000.

On the other hand, a higher sinter temperature will make the structure denser, resulting in an obstruction of the gas phase in the anode material, leading to gas transport limitation. In literature is also a formation of another phase, $\text{La}_2\text{Zr}_2\text{O}_7$, found at the LSCM/YSZ interface at sinter temperatures above 1200 °C, which leads to a higher electrode resistance [29].

LSCM sintered at 1500 °C in air is also supplied by ECN in two batches. So, as with the samples sintered at 1200 °C in air, two samples are measured that differ only in functional anode surface area. The first batch has an anode surface area of 3.8 cm² and the second batch has an anode surface area of 4.4 cm². For the rest, these samples are alike.

The fitting data on the impedance measurements of both samples can be found in Appendix 4 (sample from the first batch) and Appendix 5 (sample from the second batch).

Impedance spectroscopy data of the sample from the first batch

The first measurements at 844 °C as a function of p_{H_2} can be well modelled with the equivalent circuit $R_{\text{el}}(R_1Q_1)(R_2Q_2)(R_3Q_3)$. The first CPE has an n -value that is varying much with p_{O_2} . This n -value is in the range of 0.2 – 0.6. The second CPE shows Warburg diffusion with an n -value of a bit higher than 0.5. The third CPE has an n -value of 0.8 – 1.0. The electrolyte resistance R_{el} is independent of p_{O_2} and has a value of $7.8 \cdot 10^3 \text{ Ohm}\cdot\text{cm}$, ($1.3 \cdot 10^{-4} \text{ S}\cdot\text{cm}^{-1}$).

The measurements at 851 °C as a function of $p_{\text{H}_2\text{O}}$ are modelled with one (RQ) combination less i.e. $R_{\text{el}}(R_1Q_1)(R_2Q_2)$. The CPE's have n -values of 0.5 – 0.7 and 0.4 – 0.8 respectively. There is quite some spreading in the n -values and no specific behaviour is visible. The electrolyte resistance R_{el} is independent of p_{O_2} and has a value of 21 kOhm-cm, ($4.7 \cdot 10^{-5} \text{ S}\cdot\text{cm}^{-1}$). In literature [23]-[26], conductivity values for TZ3Y at 850 °C are in the range of $1.8 \cdot 10^{-2} - 3.0 \cdot 10^{-2} \text{ S}\cdot\text{cm}^{-1}$.

At 648 °C the data, as a function of p_{H_2} , can be modelled with the equivalent circuit $R_{\text{el}}(R_1Q_1)(R_2Q_2)(R_3Q_3)$. The R_{el} has a value of 35 kOhm-cm, ($2.9 \cdot 10^{-5} \text{ S}\cdot\text{cm}^{-1}$). The n -values corresponding to the CPE values are 0.9 – 1.0, 0.6 – 0.7 and 0.4 – 0.5.

The measurements as a function of $p_{\text{H}_2\text{O}}$ at 644 °C can be modelled with the equivalent circuit $R_{\text{el}}(R_1Q_1)(R_2Q_2)Q_3$. The n -values are 0.4 – 0.5, 0.6 – 1.0 and 0.7 – 1.0 respectively. The R_{el} has a value of 45 kOhm-cm, ($2.2 \cdot 10^{-5} \text{ S}\cdot\text{cm}^{-1}$). In literature [23]-[26], conductivity values for TZ3Y at 650 °C are in the range of $1.7 \cdot 10^{-3} - 5.1 \cdot 10^{-3} \text{ S}\cdot\text{cm}^{-1}$.

The activation energy of the electrolyte resistance is $93 \text{ kJ}\cdot\text{mol}^{-1}$ as can be seen in Figure 18. Activation energies of TZ3Y in literature [23]-[26] are in the range of $77 - 83 \pm 3 \text{ kJ}\cdot\text{mol}^{-1}$. The total electrode resistance has an activation energy of $128 \text{ kJ}\cdot\text{mol}^{-1}$.

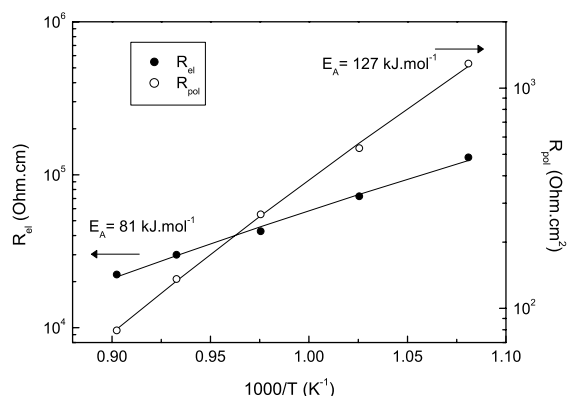


Figure 18: Activation energies of R_{el} and R_{pol} of LSCM sintered at 1500 °C in air (first batch)

In Figure 19, the pO_2 dependencies of the electrolyte resistance and the electrode polarisation at 644 °C and 844 °C are displayed. The electrolyte resistances have no strong dependency of pO_2 . There is a very strong dependency on pO_2 at the electrode polarisation as a function of pH_2 at 644 °C.

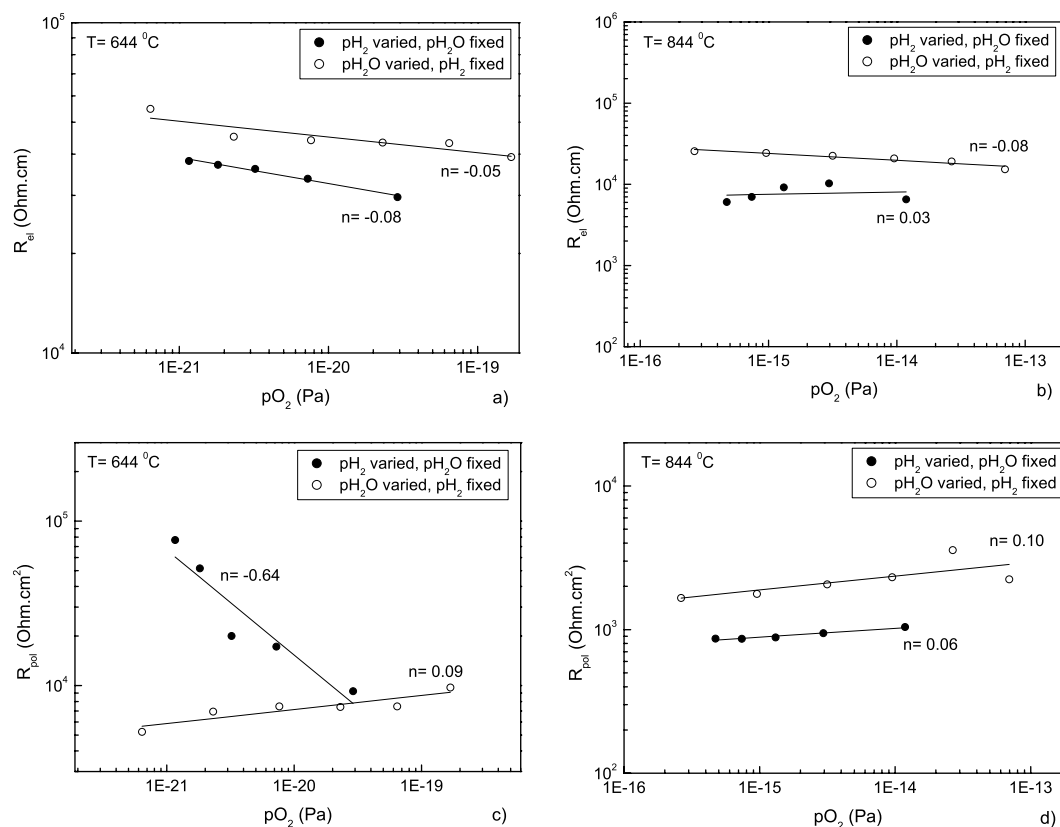


Figure 19: pO_2 dependencies of a) R_{el} at 644 °C b) R_{el} at 844 °C c) R_{pol} at 644 °C d) R_{pol} at 844 °C of LSCM sintered at 1500 °C in air (first batch).

Discussion

Electrolyte resistances are abnormally high in this sample. The electrolyte resistances are about 100 times higher than literature values. Also the electrode polarisations are very high (0.9 – 77 kOhm.cm²). Increasing the sinter temperature has not a positive effect on the properties of the symmetric cell, something that is also seen in literature [29], [19]. It is possible that the structure has become denser and is obstructing the gas phase or that

another phase is formed at the LSCM/YSZ interface (e.g. $\text{La}_2\text{Zr}_2\text{O}_7$), which both lead to higher resistances.

But it looks more like there are serious contacting problems between the cell and the platinum meshes, regarding also the results of the sample sintered at 1200°C in air. These contacting problems probably are causing a very high spreading resistance in the electrode material. Giving qualitative conclusions about the effect of an increased sinter temperature is therefore very difficult. The effects of the increased sinter temperature are probably cancelled out by the large influence of the spreading resistance.

For this reason the impedance data on the sample of the second batch sintered at 1500°C in air is not extensively discussed. Data can be found in Appendix 4. Also it was not possible to get a good fit on the measurements at 649°C as a function of $p\text{H}_2$ and $p\text{H}_2\text{O}$ for the measurements on the sample of the second batch. The latter is therefore missing in the appendix.

4.3 $\text{La}_{0.75}\text{Sr}_{0.25}\text{Cr}_{0.5}\text{Mn}_{0.5}\text{O}_{3-\delta}$ sintered at 1200°C in hydrogen

ECN has experience with perovskites sintered under a hydrogen atmosphere, resulting in better conductive properties. The LSCM symmetric cells are, for that reason, also sintered under a pure hydrogen atmosphere. Sintering took place in a Molybdenum oven at 1200°C . The partial oxygen pressure will have been very low. Only one batch of samples is measured this time, having a specific anode surface area of 4.4 cm^2 .

Impedance fitting data can be found in Appendix 5. The first measurement at 834°C as a function of partial hydrogen pressure can be modelled with the equivalent circuit $R(\text{RQ})(\text{RQ})$. The two CPE's have n-values of 0.45 and 0.90 respectively. The electrolyte resistance varies with $p\text{O}_2$ and is in the range of $36 - 56\text{ k}\Omega\cdot\text{cm}$ ($2.8\cdot 10^{-5} - 1.8\cdot 10^{-5}\text{ S}\cdot\text{cm}^{-1}$).

The measurement at 834°C as a function of partial water pressure can be modelled also with the circuit $R(\text{RQ})(\text{RQ})$. The two CPE's have n-values of 0.90 and 0.50 respectively. The second CPE therefore implies Warburg diffusion. The electrolyte resistance is independent of $p\text{O}_2$ and has a value of around $30\text{ k}\Omega\cdot\text{cm}$ ($3.4\cdot 10^{-5}\text{ S}\cdot\text{cm}^{-1}$). In literature [23]-[26], conductivity values for TZ3Y at 850°C are in the range of $1.8\cdot 10^{-2} - 3.0\cdot 10^{-2}\text{ S}\cdot\text{cm}^{-1}$.

The measurement at 647°C as a function of $p\text{H}_2$ can be modelled with the circuit $R(\text{RQ})(\text{RQ})$ (with exception of the measurement at $p\text{H}_2 = 1.98\cdot 10^4\text{ Pa}$, this particular measurement has one (RQ) extra in its model circuit). The two CPE's have n-values of 0.56 and 0.86 respectively. R_{el} is dependent of $p\text{O}_2$ and is in the range of $72 - 114\text{ k}\Omega\cdot\text{cm}$ ($1.4\cdot 10^{-5} - 8.8\cdot 10^{-6}\text{ S}\cdot\text{cm}^{-1}$).

The measurements at 647°C as a function of $p\text{H}_2\text{O}$ can be modelled with the circuit $R(\text{RQ})(\text{RQ})$ too. The two CPE's have n-values of $0.4 - 0.6$ and $0.80 - 0.9$ respectively. The electrolyte resistance R_{el} has a value of $85\text{ k}\Omega\cdot\text{cm}$ ($1.2\cdot 10^{-5}\text{ S}\cdot\text{cm}^{-1}$) and is independent of $p\text{O}_2$. In literature [23]-[26], conductivity values for TZ3Y at 650°C are in the range of $1.7\cdot 10^{-3} - 5.1\cdot 10^{-3}\text{ S}\cdot\text{cm}^{-1}$.

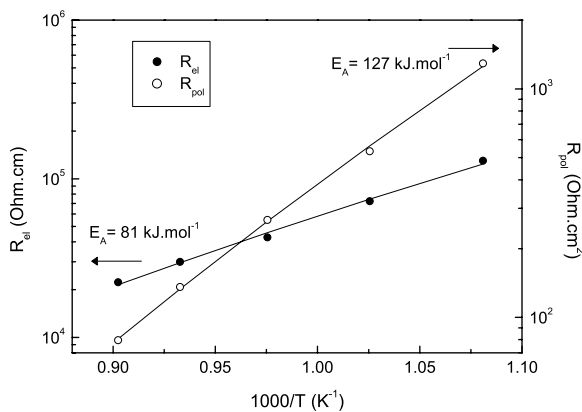


Figure 20: Activation energies of R_{el} and R_{pol} of LSCM sintered at 1200°C in hydrogen.

The activation energy of the electrolyte resistance is $81 \text{ kJ}\cdot\text{mol}^{-1}$. Activation energies of TZ3Y in literature [23]-[26] are in the range of $77 - 83 \pm 3 \text{ kJ}\cdot\text{mol}^{-1}$. The total electrode resistance has an activation energy of $147 \text{ kJ}\cdot\text{mol}^{-1}$. The activation energies are determined from Figure 20.

In Figure 21, the $p\text{O}_2$ dependencies of the electrolyte resistance and the electrode polarisation at 647°C and 834°C are displayed. The electrolyte resistances at the measurements as function of $p\text{H}_2$ have a negative dependency of $p\text{O}_2$ ($n = -0.14$). The electrode polarisations show very small dependencies of $p\text{O}_2$.

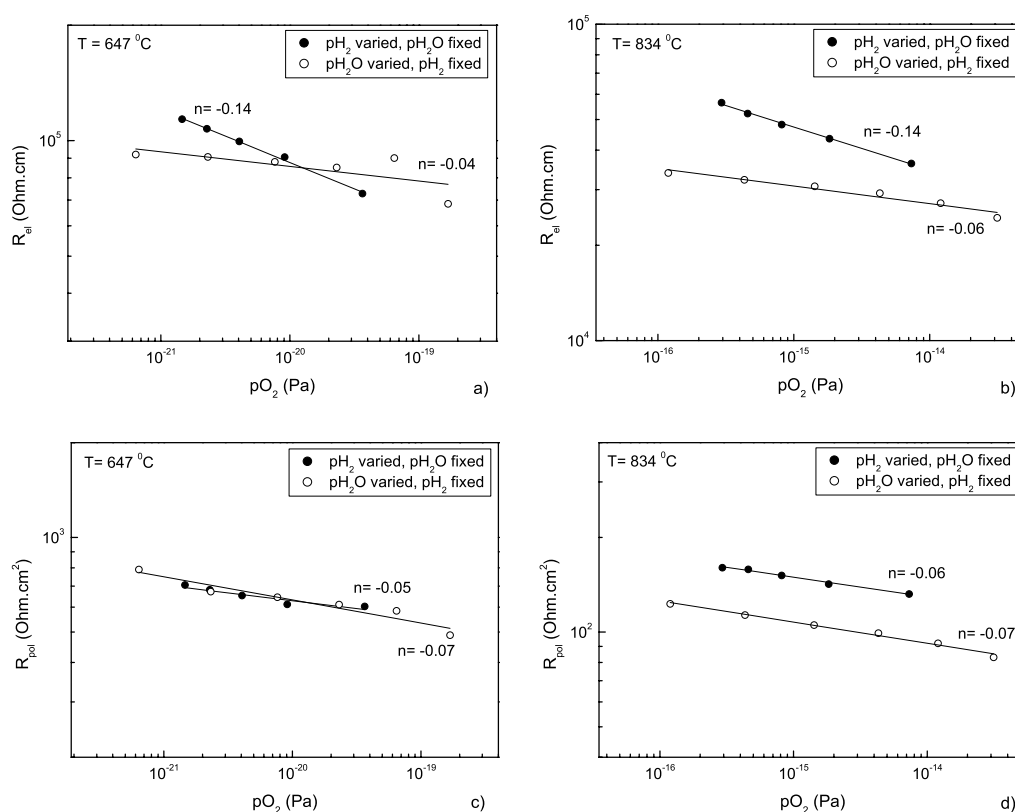


Figure 21: $p\text{O}_2$ dependencies of a) R_{el} at 647°C b) R_{el} at 834°C c) R_{pol} at 647°C d) R_{pol} at 834°C of LSCM sintered at 1200°C in hydrogen.

Discussion

No improvement in electrolyte and electrode resistances is seen on the sample that is sintered under hydrogen. Still very high resistances are measured and are now almost certainly coming from contacting problems. However, the electrode polarisations vs. $p\text{O}_2$ do show the same dependencies as a function of $p\text{H}_2$ as well as a function of $p\text{H}_2\text{O}$. This is a difference with the samples sintered in air. Bulk processes are maybe more important in this sample but it still is difficult to give conclusions about the processes because of the high resistances. The high spreading resistance shades possible influences on hydrogen sintering and it is therefore very difficult to give sharp conclusions on the possible benefits of hydrogen sintering. The next sample will be covered with a conducting layer to improve lateral conductivity at the anode surface and consequently reduce the spreading resistance.

4.4 Gold sputtered and gold painted LSCM electrodes

The appearing high electrolyte resistance is possibly caused by poor contact between the platinum meshes and the electrode layers (for lay-out, see paragraph 3.2). This can lead to bad lateral conductivity in the electrode layer and resulting in a high spreading resistance. To

enhance the contact, gold is applied on both electrode layers of the sample. If better contact can be achieved, better quantitative judgements can be made on the electrode impedance. As sample, $\text{La}_{0.75}\text{Sr}_{0.25}\text{Cr}_{0.5}\text{Mn}_{0.5}\text{O}_{3-\delta}$ sintered at $1200\text{ }^{\circ}\text{C}$ in air (second batch), is taken. This sample has a surface area of 4.4 cm^2 . Gold is chosen as the conducting layer because it has good conducting properties and a low catalytic activity (in comparison with Pt, Ag).

Gold sputtered LSCM electrodes

First, a mask is made from aluminium to cover the outer edge of the sample during sputtering. The outer edge of the sample is covered by the mask to prevent the cell from short circuiting, which will happen otherwise during the measurement when gold has created a path over the edge of the sample. The thickness of the sputtered gold layer is close to 500 nm (derived from the sputter rate and time).

In Figure 22, the first two measurements at varying $p\text{H}_2$ at $853\text{ }^{\circ}\text{C}$ are displayed. The rest of the data at varying $p\text{H}_2$ is comparable with these first two curves, but they are left out of the figure to keep the figure orderly. This figure can be compared with Figure 11 to see the influence of the gold sputtered layers on the electrodes. The symmetric cell does not differ, except for the presence of the gold layers. There can be seen that the impedance is much higher for the gold covered electrodes and that the curves are not very smooth.

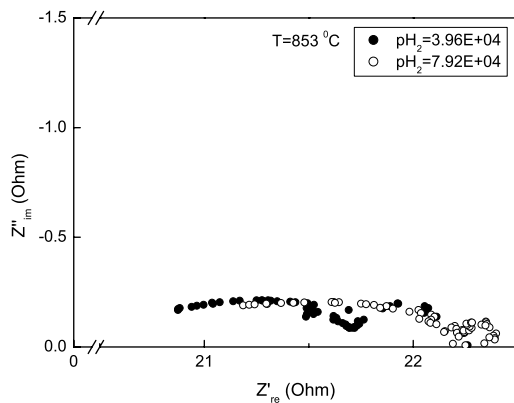


Figure 22: Impedance measurements of LSCM sintered at $1200\text{ }^{\circ}\text{C}$ in air (second batch) covered with gold by sputtering, $T=853\text{ }^{\circ}\text{C}$, $p\text{H}_2\text{O}=2.34\cdot 10^3\text{ Pa}$.

So the desired effect of enhancing the contact between the platinum meshes and electrodes does not appear from the impedance measurements. Also other data (measurements as function of $p\text{H}_2\text{O}$) show an increase in impedance with disordered data points. What exactly causes the increase in impedance is difficult to say. A possibility is that the sputtered gold completely blocks the pores in the structure of the LSCM electrode layers. The particle size of the LSCM material, sintered at $1200\text{ }^{\circ}\text{C}$, is 700 nm . The gold layer, with a thickness of 500 nm , therefore can be obstructing the gas flow into the material.

Gold painted LSCM electrodes

Gold paste was painted on the electrode surface to get more insight on the results of the sputtered gold layer and to validate the hypothesis that the sputtered gold layer blocks the pores of the electrode layers. A gold paste with a rougher structure and larger particles maybe will not have this effect. Heraeus C5007 gold paste conductor (thinner: HVS100) was applied on the electrode surface by using a small paintbrush. Next, the gold layer was dried at $150\text{ }^{\circ}\text{C}$ for 40 minutes and then fired at $850\text{ }^{\circ}\text{C}$ for 30 minutes to burn out the solvent (heating ramp $5\text{ }^{\circ}\text{C}\cdot\text{min}^{-1}$).

The measurement procedure, as described in paragraph 3.4, is applied again. Impedance fitting data can be found in Appendix 6. The first measurements are at $849\text{ }^{\circ}\text{C}$ and the $p\text{H}_2$ is varied. These measurements resulted in impedance curves that can be perfectly fit with the equivalent circuit $\text{LR}_{\text{el}}(\text{R}_1\text{Q}_1)(\text{R}_2\text{Q}_2)(\text{R}_3\text{Q}_3)$. The electrolyte resistance R_{el} is independent of $p\text{O}_2$ and has a value of $49\text{ Ohm}\cdot\text{cm}$, ($2.0\cdot 10^{-2}\text{ S}\cdot\text{cm}^{-1}$). In literature [23]-[26], conductivity values for TZ3Y at $850\text{ }^{\circ}\text{C}$ are in the range of $1.8\cdot 10^{-2} - 3.0\cdot 10^{-2}\text{ S}\cdot\text{cm}^{-1}$. There is also an inductive

element visible in these fits ($L = 2.0 \cdot 10^{-7} \Omega \cdot \text{cm}^2 \cdot \text{s}^{-1}$) and this can probably be associated to an inductive effect of the wiring and instrumentation. Further on, there are three CPE's in this circuit with n -values of 0.55, 0.8 – 1.0 and 1.0. The n -value of 0.55 is close to Warburg diffusion and the third CPE with $n=1.0$ shows capacitor behaviour.

The measurement at 849 °C as a function of $p\text{H}_2\text{O}$ can be fit with the model $R_{el}(R_1Q_1)(R_2Q_2)(R_3Q_3)$. This is the same equivalent circuit model as used at the measurements as a function of $p\text{H}_2$ at this temperature, but without the inductive element. The electrolyte resistance R_{el} is independent of $p\text{O}_2$ and has a value of 67 $\text{Ohm} \cdot \text{cm}$, ($1.5 \cdot 10^{-2} \text{ S} \cdot \text{cm}^{-1}$). In literature [23]-[26], conductivity values for TZ3Y at 850 °C are in the range of $1.8 \cdot 10^{-2} - 3.0 \cdot 10^{-2} \text{ S} \cdot \text{cm}^{-1}$. The n -values of the three CPE's are 0.8 – 1.0, 0.5 – 0.6 and 1.0 respectively. The third CPE value with the value of 1.0 shows capacitive behaviour and is found in the low frequency range. This capacitor is probably belonging to the same process seen at low frequencies at the measurement as a function of $p\text{H}_2$. The capacitance is very high at both measurements (5 – 7 F) and both R_3 -values are dependent of the partial pressures of $p\text{H}_2$ and $p\text{H}_2\text{O}$ ($n \sim -0.5$ on a log/log scale). Gas adsorption is very likely.

At 650 °C the measurements as function of $p\text{H}_2$ and $p\text{H}_2\text{O}$ both can be modelled with the equivalent circuit $R_{el}(R_1Q_1)(R_2Q_2)(R_3Q_3)(R_4Q_4)$. The electrolyte resistance is independent of $p\text{O}_2$ and is in the range of 199 – 210 $\text{Ohm} \cdot \text{cm}$ ($5.0 \cdot 10^{-3} - 4.8 \cdot 10^{-3} \text{ S} \cdot \text{cm}^{-1}$) and this goes for both type of measurements. In literature [23]-[26], conductivity values for TZ3Y at 650 °C are in the range of $1.7 \cdot 10^{-3} - 5.1 \cdot 10^{-3} \text{ S} \cdot \text{cm}^{-1}$. The four CPE's have n -values of 0.6 – 0.7, 0.5, 0.8 and 1.0 respectively. The second CPE shows Warburg diffusion. The low frequency arc is showing capacitor behaviour and has a capacitive value of about 2 – 6 F. Such high capacitances can be caused by adsorption on the anode surface, in this case hydrogen or water. R_4 has a clear dependency on the hydrogen partial pressure on a log/log scale (slope = -0.47) and a lesser dependency on the water partial pressure. So it seems like the capacitive behaviour in the low frequency range is caused by hydrogen adsorption.

The activation energy of the electrolyte resistance is 50 $\text{kJ} \cdot \text{mol}^{-1}$ as can be seen in Figure 23. Activation energies of TZ3Y in literature [23]-[26] are in the range of 77 – 83 $\pm 3 \text{ kJ} \cdot \text{mol}^{-1}$. The electrode resistance has an activation energy of 137 $\text{kJ} \cdot \text{mol}^{-1}$.

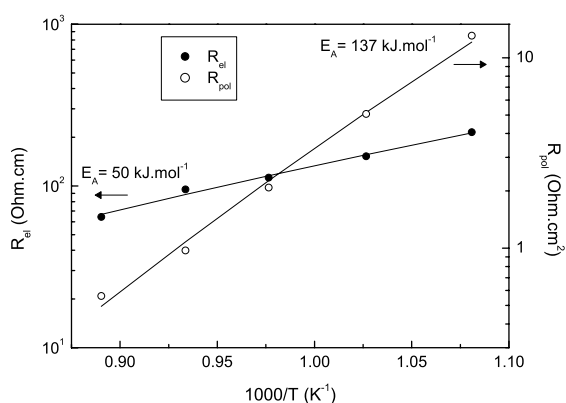


Figure 23: Activation energies of R_{el} and R_{pol} of gold paste covered LSCM sintered at 1200 °C in air.

In Figure 24, the $p\text{O}_2$ dependencies of the electrolyte resistivity and the electrode polarization at 650 °C and 850 °C are displayed. The electrolyte resistances are independent of $p\text{O}_2$.

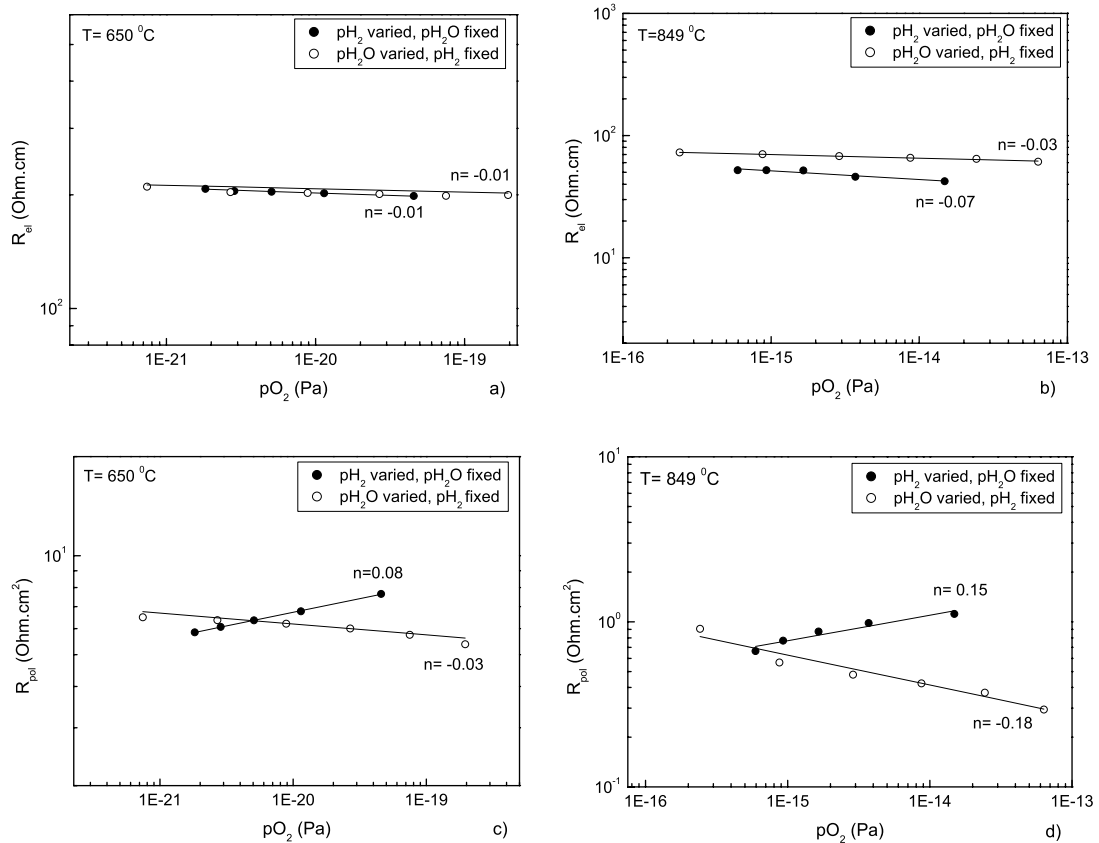


Figure 24: pO_2 dependencies of a) R_{el} at $650\text{ }^\circ\text{C}$ b) R_{el} at $849\text{ }^\circ\text{C}$ c) R_{pol} at $650\text{ }^\circ\text{C}$ d) R_{pol} at $849\text{ }^\circ\text{C}$ of gold paste covered LSCM sintered at $1200\text{ }^\circ\text{C}$ in air.

Discussion

From these measurements can be concluded that gold paste is essential for good contact. This can be seen best when these results are compared with the samples that are measured first in this research; LSCM sintered at $1200\text{ }^\circ\text{C}$ in air without a conducting gold layer. Electrolyte and electrode resistances are highly reduced and are corresponding with literature values. Tao and Irvine [18] use a gold conducting layer too and also Jiang et al. [19], [30] note the importance of such a layer.

The measured electrolyte resistance is in the range of $42 - 73\text{ Ohm}\cdot\text{cm}$ at $850\text{ }^\circ\text{C}$ ($2.3\cdot 10^{-2} - 1.4\cdot 10^{-2}\text{ S}\cdot\text{cm}^{-1}$) and matches well with the values found in literature at this temperature e.g. $1.8\cdot 10^{-2} - 3.0\cdot 10^{-2}\text{ S}\cdot\text{cm}^{-1}$ [23]-[26]. Also at $650\text{ }^\circ\text{C}$ the measured electrolyte resistance of $199 - 210\text{ Ohm}\cdot\text{cm}$ ($5.0\cdot 10^{-3} - 4.8\cdot 10^{-3}\text{ S}\cdot\text{cm}^{-1}$) corresponds well with literature ($1.7\cdot 10^{-3} - 5.1\cdot 10^{-3}\text{ S}\cdot\text{cm}^{-1}$). Usually the measured electrolyte resistance is a bit higher than expected from measurements found in literature on the electrolyte material itself because of discontinuous geometric contact at the electrode and electrolyte interface. This also goes for the electrode polarisation.

Electrode polarisation resistances of $0.37 - 1.12\text{ Ohm}\cdot\text{cm}^2$ are found in wet H_2/N_2 and values of 0.29 and $0.67\text{ Ohm}\cdot\text{cm}^2$ in wet H_2 at $850\text{ }^\circ\text{C}$. This matches quite well with values found in literature. Tao and Irvine [11],[18] report an electrode polarisation of $La_{0.75}Sr_{0.25}Cr_{0.5}Mn_{0.5}O_3$ of $0.9\text{ Ohm}\cdot\text{cm}^2$ in wet $5\%\text{ H}_2/\text{Ar}$ at $925\text{ }^\circ\text{C}$ and an electrode polarisation of $0.47\text{ Ohm}\cdot\text{cm}^2$ in wet H_2 at $925\text{ }^\circ\text{C}$. The used sinter temperature they used during LSCM preparation is not clear. A small amount of gold paste is also applied by them to enhance contact between the electrodes and the meshes. Also lower electrode polarisations are reported, but in these

cases the LSCM material is graded with YSZ or a $\text{Ce}_{0.8}\text{Gd}_{0.2}\text{O}_2$ (CGO) thin film interface layer is applied between the anode and electrolyte.

At 650 °C a big contribution of R_2 on the electrode polarisation is found. This resistance, with a corresponding CPE with $n \sim 0.5$, implies a diffusion process. At both temperatures 650 °C and 850 °C there is a process in the low frequency range, contributing to the electrode polarisation, which most likely is adsorption of hydrogen to the anode material.

This sample shows $p\text{O}_2$ dependencies on the electrode polarisation as function of $p\text{H}_2$ and $p\text{H}_2\text{O}$. Therefore, the idea is supported that surface processes mainly determine the electrode polarisation (diffusion/ adsorption of hydrogen gas) instead of bulk processes. These conclusions are also found at the sample sintered at 1200 °C in air without the gold conducting layer. Although the absolute values are not comparable, from the results on these samples with and without conducting gold layer, there can be concluded that surface processes are the most important.

4.5 Measurements at increased $p\text{O}_2$

From earlier measurements performed at ECN on cells with LSCM anodes it seems that the LSCM anode material functions better under higher partial oxygen pressure. The increase of partial oxygen pressure is also investigated here on the LSCM sample sintered at 1200 °C in air (second batch) and the gold paste covered LSCM sample sintered also at 1200 °C in air. The oxygen partial pressure is increased by reducing the hydrogen partial pressure at a high water partial pressure (see equation 4.1).

In Figure 25 and Figure 26, the results of these measurements at increased $p\text{O}_2$ are plotted. Note that there are only a few data points at higher $p\text{O}_2$, but because of the consistency between all measurements this data is expected to be trustworthy.

The effect on electrode polarisation at higher $p\text{O}_2$ is not consistent with the expectation based on the measurements at ECN. ECN performed measurements with higher $p\text{O}_2$ on complete cells with an LSCM anode, TZ3Y electrolyte and YSZ/LSM+LSM cathode and found an enhanced performance (lower polarisation resistance). However, in this case the $p\text{H}_2$ is varied to investigate the effect of an increased $p\text{O}_2$ and it can be seen that the electrode polarisation increases.

A possibility is that ECN has varied the $p\text{H}_2\text{O}$ to establish the higher $p\text{O}_2$. From Figure 25 and Figure 26 it can be seen that in the case of a higher $p\text{H}_2\text{O}$ the matching higher $p\text{O}_2$ leads to a lower electrode polarisation. However, higher $p\text{O}_2$ values could not be measured in this research due to limitations of the set-up (water baths already 60 °C at these plotted measurements). Another, less likely, possibility can be that the enhanced performance of the cell at higher $p\text{O}_2$ is dominated by another element of the cell than the anode material.

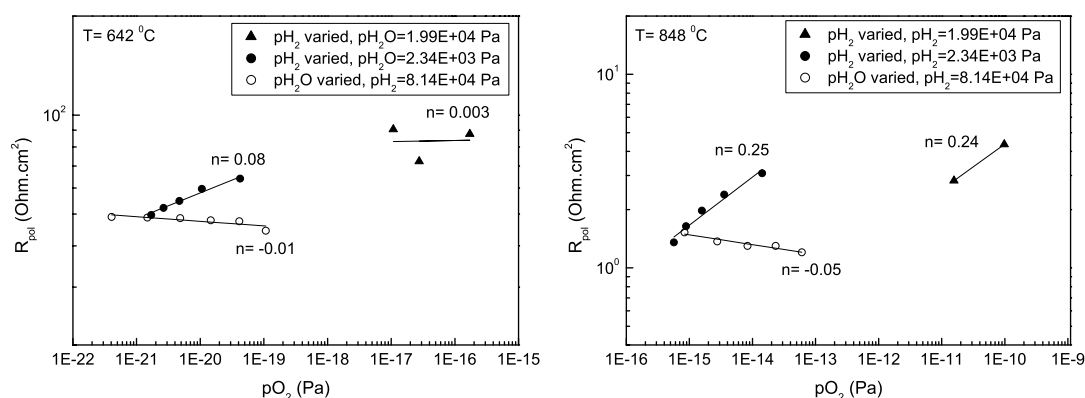


Figure 25: Measurements with increased $p\text{O}_2$ of LSCM sintered at 1200 °C in air (second batch), measured at left) 642 °C and right) 848 °C.

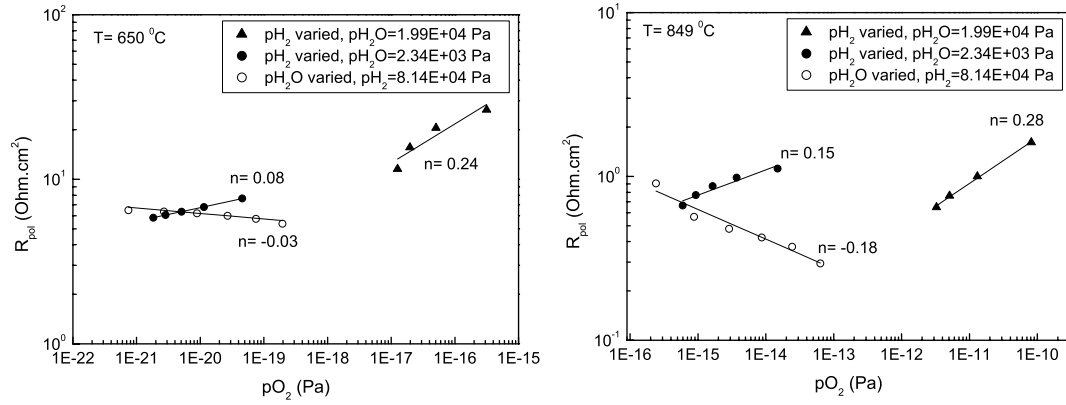


Figure 26: Measurements with increased pO_2 of gold paste covered LSCM sintered at $1200\text{ }^\circ\text{C}$ in air, measured at left) $650\text{ }^\circ\text{C}$ and right) $849\text{ }^\circ\text{C}$.

5 Conclusions and recommendations

Several samples of $\text{La}_{0.75}\text{Sr}_{0.25}\text{Cr}_{0.5}\text{Mn}_{0.5}\text{O}_3$ (LSCM) are electrochemically characterised by using Electrochemical Impedance Spectroscopy (EIS). LSCM is stated in literature [11] to be a possible alternative for Ni/YSZ composites as anode material in solid oxide fuel cells.

Symmetric cells of LSCM on a TZ3Y electrolyte, sintered at different sinter temperatures (1200°C and 1500°C) and in different sinter ambients (air and hydrogen), are characterised. These samples showed reasonable up to, more common, very high electrode polarisations in the range of $1\text{ Ohm}\cdot\text{cm}^2$ up to $77\text{ kOhm}\cdot\text{cm}^2$. Also high TZ3Y electrolyte resistances in the range of $2.5 - 56\text{ kOhm}\cdot\text{cm}$ at 850°C and $2.2 - 114\text{ kOhm}\cdot\text{cm}$ at 650°C are found. Such high electrode polarisations and electrolyte resistances are unexpected and contacting problems between the electrodes and the platinum current collectors, causing high spreading resistances, are found to be very likely.

For that reason a gold paste current collector was painted on the electrodes surfaces. The gold paste current collector improved the contact significantly, resulting in a better lateral conductivity of the anode material and a consequently lower spreading resistance. These impedance measurements also show good reproducibility.

The TZ3Y electrolyte resistance of the LSCM symmetric cell, sintered at 1200°C in air and provided with a conducting gold layer, is then measured to be $42 - 73\text{ Ohm}\cdot\text{cm}$ ($2.3\cdot 10^{-2} - 1.4\cdot 10^{-2}\text{ S}\cdot\text{cm}^{-1}$) at 850°C and $199 - 210\text{ Ohm}\cdot\text{cm}$ ($5.0\cdot 10^{-3} - 4.8\cdot 10^{-3}\text{ S}\cdot\text{cm}^{-1}$) at 650°C . This matches very well with conductivity values in literature for TZ3Y, where values are reported of $1.8\cdot 10^{-2} - 3.0\cdot 10^{-2}\text{ S}\cdot\text{cm}^{-1}$ and $1.7\cdot 10^{-3} - 5.1\cdot 10^{-3}\text{ S}\cdot\text{cm}^{-1}$ respectively for 850°C and 650°C [23]-[26]. Usually the measured electrolyte resistance is a bit higher than expected from measurements found in literature on the electrolyte material itself because of discontinuous geometric contact at the electrode and electrolyte interface. This theory also goes for the electrode polarisation. This is not really an issue in these results though.

While these values for the electrolyte resistances are corresponding well with literature, there can be concluded that the contact between electrode and current collector is improved and that the measured electrode polarisation is representative for the electrode processes. For the sample sintered at 1200°C in air with the conducting gold layer, electrode polarisation resistances of $0.37 - 1.12\text{ Ohm}\cdot\text{cm}^2$ are found in different wet H_2/N_2 compositions at 850°C and values of 0.29 and $0.67\text{ Ohm}\cdot\text{cm}^2$ are found in wet H_2 at 850°C . This matches quite well with values found in literature. Tao and Irvine [11],[18] report an electrode polarisation of $\text{La}_{0.75}\text{Sr}_{0.25}\text{Cr}_{0.5}\text{Mn}_{0.5}\text{O}_3$ of $0.9\text{ Ohm}\cdot\text{cm}^2$ in wet $5\%\text{ H}_2/\text{Ar}$ at 925°C and an electrode polarisation of $0.47\text{ Ohm}\cdot\text{cm}^2$ in wet H_2 at 925°C .

These performances are considered to be close to the electrode performance of Ni/YSZ cermet anodes. According to Primdahl [31] electrode polarisation resistances in the order of $0.15 - 0.30\text{ Ohm}\cdot\text{cm}^2$ are frequently reported for Ni/YSZ at 1000°C in wet H_2 .

Tao and Irvine did also use a gold layer to improve the contact between electrode and current collector. It can be concluded that using a conducting gold layer is essential for impedance measurements on these symmetric cells. The importance of such a layer is also stated by Jiang et al. [19], [30].

The sample sintered at 1200°C in air with the conducting gold paste layer is further characterised and at 650°C a big contribution of a certain resistance on the electrode polarisation is found. This resistance belongs to a (RQ) element in the equivalent circuit and has a corresponding CPE with $n\sim 0.5$. This process implies a Warburg diffusion process.

At both temperatures 650°C and 850°C there is a process in the low frequency range, contributing to the electrode polarisation, which most likely is dissociative adsorption of hydrogen onto the anode material. This process is described by an (RQ) element with a corresponding CPE with $n\sim 1.0$ and high capacitances of around 1.7 to 7.7 Farad . Such high capacitances are likely to be assigned to adsorption processes. Also the resistance, belonging to this process, is dependent on the hydrogen partial pressure on a log/log scale with a slope of $n=-0.47$. Because of the strong dependency on the $p\text{H}_2$ the hypothesis that this process is dissociative adsorption of hydrogen becomes more plausible.

This sample also shows different pO_2 dependencies on the electrode polarisation as function of pH_2 and pH_2O . Therefore, the idea is supported that surface processes mainly determine the electrode polarisation (diffusion/ adsorption of hydrogen gas) instead of bulk processes.

These conclusions are also found at the sample sintered at $1200\text{ }^\circ\text{C}$ in air without the gold conducting layer. Although the absolute values are not comparable, from the results on these samples with and without conducting gold layer, there can be concluded that surface processes are the most important processes in LSCM electrodes instead of bulk processes.

Measurements at increased oxygen partial pressure up to 10^{-11} Pa are performed. The effect on electrode polarisation at higher pO_2 is not consistent with the expectation based on the measurements at ECN. ECN performed measurements with higher pO_2 on complete cells with an LSCM anode, TZ3Y electrolyte and YSZ/LSM+LSM cathode and found an enhanced performance (lower polarisation resistance). However, in this research the pH_2 is varied to investigate the effect of an increased pO_2 and it can be seen that the electrode polarisation increases. A possibility is that ECN has varied the pH_2O to establish the higher pO_2 . From measurements can be seen that in the case of a higher pH_2O the matching higher pO_2 does lead to a lower electrode polarisation. However, much higher pH_2O values could not be reached in this research due to limitations of the set-up.

Although electrochemical impedance spectroscopy gives a lot of information about the samples and the corresponding electrochemical processes under operation conditions, it is not suitable as a technique on its own for completely characterising this material. Therefore, it is highly recommended that Scanning Electron Microscopy (SEM) pictures are made of the complete cells to investigate the microstructure before testing as well as after testing them. Conclusions can be made on the morphology of the electrode/electrolyte interface and, if combined with Energy Dispersive X-ray Spectroscopy (EDX or EDS), about the composition of the material before and after testing. The latter technique can especially be useful in combination with SEM to see if other phases are formed (e.g. $La_2Zr_2O_7$). This can be supported by X-Ray Diffraction (XRD) measurements. SEM pictures are also useful to see how the surfaces of the gold paste covered electrodes look like and how far the gold penetrated the electrode layers.

Sometimes after the measurements, a black powder was found as residue in the quartz tube. A possibility is that this powder is a chromium-based compound, coming from the LSCM layers. If this is the case, then the material is not stable under the operating temperature. This should be checked by analysing the powder with XRD. In literature nothing is found on the formation of such a compound under operating conditions.

Another recommendation is to repeat the measurements of the cells that are produced under higher sinter temperatures and cells that are sintered under a hydrogen atmosphere, but now with applying also a conducting gold layer on these cells. Maybe more qualitative conclusions can be given about the sinter parameters on the electrochemical processes that take place in these cells when a gold layer is ensuring the contact between electrodes and current collectors. Although in literature $1200\text{ }^\circ\text{C}$ is often referred to as optimal sinter temperature for this anode material [19], [29]. But for the fundamental research on this material it is certainly very useful.

6 Dankwoord

Klaar! Hier ligt dan het resultaat van de laatste opdracht die ik als student Chemische Technologie heb volbracht. Maar voordat u dit verslag terzijde legt, wil ik nog graag deze gelegenheid benutten om wat mensen te bedanken die aan mijn afstudeerperiode hebben bijgedragen.

Ten eerste wil ik graag Bernard en Henny bedanken voor het enthousiasme en de goede tips tijdens mijn afstudeeropdracht en voor de begeleiding op zich naast jullie drukke agenda's. Daarnaast wil ik Bernard nog in het bijzonder bedanken voor het mogelijk maken van het bezoek aan de zomerschool in Zwitserland tijdens mijn afstudeerperiode. Deze zomerschool was niet alleen vakinhoudelijk heel nuttig betreffende de lezingen, maar ik heb ook veel geleerd van de gesprekken buiten de lezingen om met de verschillende PhD-studenten die in Europa werkzaam zijn op het gebied van vaste-stof brandstofcellen. En Henny wil ik naast het begeleiden van deze opdracht ook nog in het bijzonder bedanken voor het aandragen van contactgegevens voor een stageopdracht bij ABB Corporate Research in Zwitserland destijds. Deze stage was ook een geweldige ervaring!

Tevens bedank ik:

- De rest van mijn D-commissie: Dave Blank, Barbara Mojet en Frans van Berkel voor zitting in mijn afstudeercommissie, het mogelijk maken van deze gecombineerde opdracht bij AMK en ECN en het kritisch lezen van mijn verslag.
- Guillaume Schoemakers van ECN voor het prepareren van de samples.
- De gezellige AMK groep en daarbij met name Henk, Gerrit, en Mieke voor hun hulp bij de apparatuur op het lab en Frank voor de hulp bij o.a. het sputteren.
- Mijn kamergenoten Wouter, Peter, Gabriella (en daarvoor ook Michiel, Michael, Song en Jetske) voor de uitstekende sfeer in de studentenkamer. En de afstudeerders Hans, Daniël, Martin, Tijs, Matthijs en Gé die bijna dagelijks bij de pooltafel te vinden waren tijdens de lunch.
- Mijn huisgenoten aan de Nachtegaalstraat René, Rijk, Lodewijk (en later ook Huub) voor hun interesse in mijn werkzaamheden op CT en natuurlijk de gezelligheid in huis.

En *last* maar zeker *not least* bedank ik mijn familie en de rest van mijn vrienden en in het bijzonder mijn ouders en Jolanda voor de geweldige steun tijdens mijn afstuderen en de rest van mijn studie!

Zo, en dan is het nu tijd voor de volgende uitdaging! Waar die dan ook moge zijn.

Raymon

7 Literature

- [1] Boudghene Stambouli A., Traversa E., *Solid oxide fuel cells (SOFCs): a review of an environmentally clean and efficient source of energy*, Renewable and Sustainable Energy Reviews, 6, **2002**, 433-455.
- [2] Minh N.Q., *Ceramic Fuel Cells*, Journal of the American Ceramic Society, 76 (3), **1993**, 563-588.
- [3] Hoogers G., *Fuel cell technology handbook*, CRC Press LLC, Florida, **2003**.
- [4] <http://www.risoe.dk>, last viewed November **2005**.
- [5] S.C. Singhal, K. Kendall, *High temperature solid oxide fuel cells: fundamentals, design and applications*, Elsevier, Oxford, UK, **2003**.
- [6] Singh P., Minh N.Q., *Solid oxide fuel cells: Technology status*, International Journal of Applied Ceramic Technology, 1, **2004**, 5-15.
- [7] Perry M.L., Fuller T.F., *A historical perspective of fuel cell technology in the 20th century*, Journal of the Electrochemical Society, 149, 7, **2002**, S59-S67.
- [8] Minh N.Q., *Solid oxide fuel cell technology – features and applications*, Solid State Ionics, 174, **2004**, 271-277.
- [9] Yamamoto O., *Solid oxide fuel cells: fundamental aspects and prospects*, Electrochimica Acta, 45, **2000**, 2423-2435.
- [10] Zha S., Tsang P., Cheng Z., Liu M., *Electrical properties and sulfur tolerance of $La_{0.75}Sr_{0.25}Cr_{1-x}Mn_xO_3$ under anodic conditions*, Journal of Solid State Chemistry, 178, **2005**, 1844-1850.
- [11] Tao S., Irvine J.T.S., *A redox-stable efficient anode for solid-oxide fuel cells*, Nature Materials, 2, **2003**, 320-323.
- [12] <http://www.fuelcells.org>, last viewed November **2005**.
- [13] Jiang S.P., Chan S.H., *A review of anode materials development in solid oxide fuel cells*, Journal of Material Science, 39, **2004**, 4405-4439.
- [14] McIntosh S., Gorte R.J., *Direct hydrocarbon solid oxide fuel cells*, Chem. Rev., 104, **2004**, 4845-4865.
- [15] Tao S., Irvine J.T.S., *Discovery and characterisation of novel oxide anodes for solid oxide fuel cells*, The Chemical Record, 4, **2004**, 83-95.
- [16] Liu J., Madsen B.D, Ji Z., Barnett S.A., *A fuel-flexible ceramic-based anode for solid oxide fuel cells*, Electrochemical and Solid State Letters, 5, (6), **2002**, A122-A124.
- [17] Zhu W.Z., Deevi S.C., *A review on the status of anode materials for solid oxide fuel cells*, Materials Science and Engineering, A362, **2003**, 228-239.
- [18] Tao S., Irvine J.T.S., *Synthesis and characterization of $(La_{0.75}Sr_{0.25})Cr_{0.5}Mn_{0.5}O_{3-\delta}$ a redox-stable, efficient perovskite anode for SOFCs*, Journal of the Electrochemical Society, 151, (2), **2004**, A252-A259.
- [19] Jiang S.P., Chen X.J., Chan S.H., Kwok J.T., Khor K.A., *$(La_{0.75}Sr_{0.25})(Cr_{0.5}Mn_{0.5})O_3/YSZ$ composite anodes for methane oxidation reaction in solid oxide fuel cells*, Solid State Ionics, 177, **2006**, 149-157.
- [20] Boukamp B.A., *Introduction to electrochemical impedance spectroscopy*, 2nd RealSOFC Summerschool in Ovronnaz, Switzerland, September **2005**.
- [21] Gamry Instruments, *Fundamentals of electrochemical impedance spectroscopy*, <http://www.gamry.com>, last viewed September **2005**.
- [22] Barsoukov E., Macdonald J.R., *Impedance spectroscopy: theory, experiment and applications*, 2nd edition, Wiley-Interscience, Hoboken, New Jersey, **2005**.
- [23] Badwal S.P.S., Ciacchi F.T., Giampietro K.M., *Analysis of the conductivity of commercial easy sintered grade 3 mol% Y_2O_3 - ZrO_2 materials*, Solid State Ionics, 176, **2005**, 169-178.
- [24] Weller M., Herzog R., Kilo M., Borchardt G., Weber S., Scherrer S., *Oxygen mobility in yttria-doped zirconia studied by internal friction, electrical conductivity and tracer diffusion experiments*, Solid State Ionics, 175, **2004**, 409-413.
- [25] Badwal S.P.S., *Zirconia-based solid electrolytes: microstructure, stability and ionic conductivity*, Solid State Ionics, 52, **1992**, 23-32.
- [26] Ciacchi F.T., Crane K.M., Badwal S.P.S., *Evaluation of commercial zirconia powders for solid oxide fuel cells*, Solid State Ionics, 73, **1994**, 49-61.

- [27] Skaarup S., Zachau-Christiansen B., Jacobsen T., *Surface species and surface mobility on Ni/YSZ anodes*, Proceedings of the 17th Risoe International Symposium on Materials Science: High Temperature Electrochemistry: Ceramics and Materials, **1996**, 423-430.
- [28] Bieberle A., Meier L.P., Gauckler L.J., *The electrochemistry of Ni pattern anodes used as solid oxide fuel cell model electrodes*, Journal of the electrochemical society, 148, 6, **2001**, A646-A656.
- [29] Chen X.J., Khor K.A., Chan S.H., *Performance of (La,Sr)(Cr,Mn)O₃ anode for direct oxidation of methane in solid oxide fuel cell*, School of mechanical and production engineering, Nanyang Technological University, Singapore.
- [30] Jiang S.P., Love J.G., Apateanu L., *Effect of contact between electrode and current collector on the performance of solid oxide fuel cells*, Solid State Ionics, 160, **2003**, 15-26.
- [31] Primdahl S., *Nickel/yttria-stabilised zirconia cermet anodes for solid oxide fuel cells*, PhD-Thesis, University of Twente, the Netherlands, **1999**, 186-187.

Appendices

Appendix 1 – Equivalent circuit modelling data of LSCM sintered at 1200 °C in air (sample from first batch)

Measurements as function of $p\text{H}_2$

		T 840 °C		pH ₂ O 2.34E+03 Pa											
CDC	pH ₂ (Pa)	ChiSq	R _{el} (Ω)	R ₁ (Ω)	Q ₁ (Ω ⁻¹ .s ⁿ)	n ₁	R ₂ (Ω)	Q ₂ (Ω ⁻¹ .s ⁿ)	n ₂	R ₃ (Ω)	Q ₃ (Ω ⁻¹ .s ⁿ)	n ₃	R ₄ (Ω)	Q ₄ (Ω ⁻¹ .s ⁿ)	n ₄
R(RQ)(RQ)	1.98E+04	3.8E-06	14.90	5.18	0.16	0.50	-	-	-	2.25	1.09	1.00	37	0.37	0.98
R(RQ)(RQ)(RQ)	3.96E+04	9.5E-07	14.39	0.61	0.16	0.50	3.13	0.17	0.66	2.06	1.02	1.00	33	0.33	0.96
R(RQ)(RQ)(RQ)	5.94E+04	9.4E-07	14.16	1.07	0.16	0.49	2.04	0.21	0.76	1.61	1.05	1.00	34	0.26	0.91
R(RQ)(RQ)(RQ)	7.92E+04	7.1E-07	14.16	1.18	0.16	0.48	1.60	0.22	0.80	1.30	1.01	1.00	34	0.22	0.87
R(RQ)(RQ)(RQ)	9.90E+04	6.1E-07	14.01	1.15	0.15	0.48	1.56	0.21	0.81	1.12	1.11	1.00	28	0.31	0.93

pO ₂ (Pa)	R _{el} (Ω.cm)	R ₁ (Ω.cm ²)	R ₂ (Ω.cm ²)	R ₃ (Ω.cm ²)	R _{pol} (Ω.cm ²)
9.79E-15	4358	9.9	-	4.3	14.1
2.45E-15	4209	1.2	5.9	3.9	11.0
1.09E-15	4140	2.0	3.9	3.1	9.0
6.12E-16	4140	2.2	3.0	2.5	7.8
3.92E-16	4096	2.2	3.0	2.1	7.3

		T 650 °C		pH ₂ O 2.34E+03 Pa											
CDC	pH ₂ (Pa)	ChiSq	R _{el} (Ω)	R ₁ (Ω)	Q ₁ (Ω ⁻¹ .s ⁿ)	n ₁	R ₂ (Ω)	Q ₂ (Ω ⁻¹ .s ⁿ)	n ₂	R ₃ (Ω)	Q ₃ (Ω ⁻¹ .s ⁿ)	n ₃	R ₄ (Ω)	Q ₄ (Ω ⁻¹ .s ⁿ)	n ₄
R(RQ)(RQ)(RQ)(RQ)	1.98E+04	1.4E-06	90	30	8.17E-05	0.57	50	1.19E-03	0.72	152	5.21E-03	0.51	37	0.37	0.98
R(RQ)(RQ)(RQ)(RQ)	3.96E+04	1.2E-06	100	35	7.69E-05	0.55	51	1.02E-03	0.75	147	4.54E-03	0.53	33	0.33	0.96
R(RQ)(RQ)(RQ)(RQ)	5.94E+04	1.2E-06	107	40	8.14E-05	0.51	52	1.02E-03	0.76	138	4.65E-03	0.56	34	0.26	0.91
R(RQ)(RQ)(RQ)(RQ)	7.92E+04	1.2E-06	103	48	8.94E-05	0.47	49	9.99E-04	0.77	131	4.61E-03	0.57	34	0.22	0.87
R(RQ)(RQ)(RQ)(RQ)	9.90E+04	1.1E-06	111	47	9.01E-05	0.48	53	9.64E-04	0.77	129	4.85E-03	0.56	28	0.31	0.93

pO ₂ (Pa)	R _{el} (Ω.cm)	R ₁ (Ω.cm ²)	R ₂ (Ω.cm ²)	R ₃ (Ω.cm ²)	R ₄ (Ω.cm ²)	R _{pol} (Ω.cm ²)
4.56E-20	26388	57	95	290	70	512
1.14E-20	29342	67	96	280	62	506
5.07E-21	31266	77	99	262	66	503
2.85E-21	30250	91	94	248	66	499
1.83E-21	32559	89	100	245	53	486

Measurements as function of pH₂O

T 841 °C
pH₂ 8.14E+04 Pa

CDC	pH ₂ O (Pa)	ChiSq	R _{tot} (Ω)	R ₁ (Ω)	Q ₁ (Ω ⁻¹ .s ⁿ)	n ₁	R ₂ (Ω)	Q ₂ (Ω ⁻¹ .s ⁿ)	n ₂	T _{H₂O} (°C)
R(RQ)(RQ)	1.99E+04	3.5E-06	8.8	1.42	0.11	0.61	1.73	0.29	0.88	60
R(RQ)(RQ)	1.23E+04	2.8E-06	12.0	1.40	0.15	0.53	1.95	0.28	0.84	50
R(RQ)(RQ)	7.37E+03	1.8E-06	11.5	1.34	0.13	0.52	1.74	0.28	0.85	40
R(RQ)(RQ)	4.24E+03	1.6E-06	12.9	1.41	0.16	0.50	1.86	0.30	0.83	30
R(RQ)(RQ)	2.34E+03	1.6E-06	13.3	1.25	0.16	0.49	1.88	0.31	0.80	20
R(RQ)(RQ)	1.23E+03	2.1E-06	13.8	1.26	0.21	0.47	1.80	0.42	0.74	10

pO ₂ (Pa)	R _{tot} (Ω.cm)	R ₁ (Ω.cm ²)	R ₂ (Ω.cm ²)	R _{pol} (Ω.cm ²)
4.39E-14	2571	2.7	3.3	6.0
1.69E-14	3521	2.7	3.7	6.4
6.03E-15	3364	2.6	3.3	5.9
1.99E-15	3760	2.7	3.5	6.2
6.05E-16	3876	2.4	3.6	6.0
1.67E-16	4021	2.4	3.4	5.8

T 650 °C
pH₂ 8.14E+04 Pa

CDC	pH ₂ O (Pa)	ChiSq	R _{tot} (Ω)	R ₁ (Ω)	Q ₁ (Ω ⁻¹ .s ⁿ)	n ₁	R ₂ (Ω)	Q ₂ (Ω ⁻¹ .s ⁿ)	n ₂	R ₃ (Ω)	Q ₃ (Ω ⁻¹ .s ⁿ)	n ₃	R ₄ (Ω)	Q ₄ (Ω ⁻¹ .s ⁿ)	n ₄
R(RQ)(RQ)(RQ)(RQ)	1.99E+04	2.2E-06	106	42	8.2E-05	0.49	41	1.3E-03	0.74	113	6.5E-03	0.56	25	0.42	1.00
R(RQ)(RQ)(RQ)(RQ)	1.23E+04	8.8E-07	116	50	7.0E-05	0.48	43	1.1E-03	0.77	132	5.5E-03	0.53	43	0.26	0.93
R(RQ)(RQ)(RQ)(RQ)	7.37E+03	1.1E-06	107	62	4.6E-05	0.47	40	1.2E-03	0.77	135	6.1E-03	0.52	39	0.35	0.99
R(RQ)(RQ)(RQ)(RQ)	4.24E+03	7.4E-07	148	25	7.7E-05	0.61	48	1.1E-03	0.75	131	6.0E-03	0.54	51	0.25	0.92
R(RQ)(RQ)(RQ)(RQ)	2.34E+03	1.0E-06	117	60	5.1E-05	0.47	47	1.1E-03	0.77	131	5.9E-03	0.54	50	0.27	0.96
R(RQ)(RQ)(RQ)(RQ)	1.23E+03	1.1E-06	121	59	8.2E-05	0.43	47	1.1E-03	0.77	128	6.0E-03	0.55	54	0.23	0.92

pO ₂ (Pa)	R _{tot} (Ω.cm)	R ₁ (Ω.cm ²)	R ₂ (Ω.cm ²)	R ₃ (Ω.cm ²)	R ₄ (Ω.cm ²)	R _{pol} (Ω.cm ²)
1.95E-19	31029	80	78	214	48	420
7.49E-20	34048	95	82	251	82	511
2.68E-20	31251	117	75	257	75	525
8.86E-21	43377	47	91	249	97	484
2.69E-21	34323	114	90	249	95	548
7.42E-22	35432	112	90	244	103	549

Temperature dependency

pH₂ 9.90E+04 Pa
pH₂O 2.34E+03 Pa

CDC	T (°C)	ChiSq	R _{el} (Ω)	R ₁ (Ω)	Q ₁ (Ω ⁻¹ .s ⁿ)	n ₁	R ₂ (Ω)	Q ₂ (Ω ⁻¹ .s ⁿ)	n ₂	R ₃ (Ω)	Q ₃ (Ω ⁻¹ .s ⁿ)	n ₃
R(RQ)Q	648	4.1E-06	30.5	18.1	8.1E-06	0.84	292.8	0.09	0.36	-	-	-
R(RQ)(RQ)(RQ)	699	3.5E-06	19.1	8.1	8.6E-06	0.82	15.5	0.10	0.45	6.4	1.15	0.94
R(RQ)(RQ)(RQ)	752	3.1E-06	11.2	5.2	6.6E-06	0.76	3.9	0.11	0.51	4.2	0.41	0.85
R(RQ)(RQ)(RQ)	804	1.8E-06	5.4	5.4	3.5E-06	0.66	1.5	0.13	0.55	2.2	0.29	0.82
R(RQ)(RQ)	854	1.7E-06	7.3	-	-	-	0.6	0.17	0.51	1.5	0.23	0.70

1000/T (K ⁻¹)	R _{el} (Ω.cm)	R ₁ (Ω.cm ²)	R ₂ (Ω.cm ²)	R ₃ (Ω.cm ²)	R _{pol} (Ω.cm ²)
1.09	8925	34.5	556.6	-	591.0
1.03	5584	15.4	29.5	12.2	57.1
0.98	3273	10.0	7.5	8.0	25.5
0.93	1565	10.2	2.8	4.2	17.2
0.89	2133	-	1.1	2.9	4.0

E_A =

68.6	65.6	246.4	82.88	184.51
------	------	-------	-------	--------

 kJ.mol⁻¹

Appendix 2 – Equivalent circuit modelling data of LSCM sintered at 1200 °C in air (sample from second batch)

Measurements as function of p_{H_2}

T 848 °C
 p_{H_2O} 2.34E+03 Pa

CDC	p_{H_2} (Pa)	ChiSq	R_{sei} (Ω)	R_1 (Ω)	Q_1 ($\Omega^{-1} \cdot s^n$)	n_1	R_2 (Ω)	Q_2 ($\Omega^{-1} \cdot s^n$)	n_2
R(RQ)(RQ)	1.98E+04	2.7E-07	8.5	0.70	0.33	0.51	0.70	1.85	0.94
R(RQ)(RQ)	3.96E+04	1.4E-07	9.3	0.60	0.34	0.50	0.49	2.22	0.95
R(RQ)(RQ)	5.94E+04	9.2E-08	9.8	0.53	0.34	0.50	0.37	2.60	0.95
R(RQ)(RQ)	7.92E+04	5.5E-08	10.3	0.50	0.33	0.51	0.25	3.06	0.98
R(RQ)(RQ)	9.90E+04	1.6E-08	10.7	0.47	0.31	0.51	0.15	3.90	1.00

pO_2 (Pa)	R_{sei} ($\Omega \cdot cm$)	R_1 ($\Omega \cdot cm^2$)	R_2 ($\Omega \cdot cm^2$)	R_{pol} ($\Omega \cdot cm^2$)
1.42E-14	2870	1.55	1.54	3.09
3.55E-15	3152	1.32	1.08	2.40
1.58E-15	3335	1.17	0.81	1.98
8.87E-16	3488	1.09	0.55	1.64
5.67E-16	3628	1.03	0.32	1.35

T 649 °C
 p_{H_2O} 2.34E+03 Pa

CDC	p_{H_2} (Pa)	ChiSq	R_{sei} (Ω)	R_1 (Ω)	Q_1 ($\Omega^{-1} \cdot s^n$)	n_1	R_2 (Ω)	Q_2 ($\Omega^{-1} \cdot s^n$)	n_2	R_3 (Ω)	Q_3 ($\Omega^{-1} \cdot s^n$)	n_3
R(RQ)(RQ)(RQ)	1.98E+04	3.6E-07	30	2.38	4.8E-04	0.64	2.11	2.8E-03	0.70	10.0	0.13	0.55
R(RQ)(RQ)(RQ)	3.96E+04	2.5E-07	35	2.55	3.8E-04	0.66	2.21	2.5E-03	0.71	8.8	0.13	0.56
R(RQ)(RQ)(RQ)	5.94E+04	6.8E-07	37	1.71	1.3E-04	0.78	3.22	2.6E-03	0.63	7.5	0.12	0.60
R(RQ)(RQ)(RQ)	7.92E+04	3.0E-07	39	1.99	1.7E-04	0.74	3.10	2.7E-03	0.64	6.7	0.12	0.61
R(RQ)(RQ)(RQ)	9.90E+04	3.3E-07	41	1.86	1.3E-04	0.77	3.33	2.7E-03	0.62	6.1	0.12	0.64

pO_2 (Pa)	R_{sei} ($\Omega \cdot cm$)	R_1 ($\Omega \cdot cm^2$)	R_2 ($\Omega \cdot cm^2$)	R_3 ($\Omega \cdot cm^2$)	R_{pol} ($\Omega \cdot cm^2$)
4.23E-20	10255	11	9	44	64
1.06E-20	11745	11	10	39	60
4.70E-21	12700	8	14	33	55
2.65E-21	13337	9	14	30	52
1.69E-21	13867	8	15	27	50

Measurements as function of pH₂O

T 848 °C
pH₂ 8.14E+04 Pa

CDC	pH ₂ O (Pa)	ChiSq	R _{el} (Ω)	R ₁ (Ω)	Q ₁ (Ω ⁻¹ .s ⁿ)	n ₁	R ₂ (Ω)	Q ₂ (Ω ⁻¹ .s ⁿ)	n ₂	R ₃ (Ω)	Q ₃ (Ω ⁻¹ .s ⁿ)	n ₃	T _{H2O} (°C)
R(RQ)(RQ)(RQ)	1.99E+04	4.3E-07	7.6	0.08	0.10	0.54	0.33	0.18	0.65	0.14	1.17	0.96	60
R(RQ)(RQ)(RQ)	1.23E+04	1.0E-07	8.0	0.07	0.10	0.50	0.36	0.21	0.63	0.15	1.45	0.97	50
R(RQ)(RQ)(RQ)	7.37E+03	3.9E-08	8.3	0.09	0.18	0.45	0.33	0.22	0.65	0.17	1.63	0.91	40
R(RQ)(RQ)(RQ)	4.24E+03	8.1E-08	8.5	0.08	0.14	0.48	0.38	0.24	0.62	0.17	2.19	0.93	30
R(RQ)(RQ)(RQ)	2.34E+03	3.5E-08	9.2	0.05	0.07	0.57	0.41	0.28	0.57	0.23	3.21	0.97	20

pO ₂ (Pa)	R _{el} (Ω.cm)	R ₁ (Ω.cm ²)	R ₂ (Ω.cm ²)	R ₃ (Ω.cm ²)	R _{pool} (Ω.cm ²)
6.07E-14	2581	0.17	0.73	0.30	1.20
2.33E-14	2723	0.16	0.80	0.34	1.30
8.33E-15	2804	0.19	0.73	0.38	1.30
2.76E-15	2899	0.17	0.83	0.37	1.37
8.37E-16	3109	0.11	0.91	0.51	1.53

T 642 °C
pH₂ 8.14E+04 Pa

CDC	pH ₂ O (Pa)	ChiSq	R _{el} (Ω)	R ₁ (Ω)	Q ₁ (Ω ⁻¹ .s ⁿ)	n ₁	R ₂ (Ω)	Q ₂ (Ω ⁻¹ .s ⁿ)	n ₂	R ₃ (Ω)	Q ₃ (Ω ⁻¹ .s ⁿ)	n ₃	T _{H2O} (°C)
R(RQ)(RQ)(RQ)	1.99E+04	2.5E-06	30	0.68	4.07E-05	1.00	3.9	2.54E-03	0.61	5.5	0.13	0.66	60
R(RQ)(RQ)(RQ)	1.23E+04	8.9E-07	32	1.56	2.90E-04	0.71	3.2	2.67E-03	0.64	6.0	0.12	0.65	50
R(RQ)(RQ)(RQ)	7.37E+03	4.8E-07	34	1.33	1.55E-04	0.78	3.5	2.58E-03	0.62	6.1	0.12	0.65	40
R(RQ)(RQ)(RQ)	4.24E+03	4.2E-07	34	1.40	1.62E-04	0.78	3.5	2.60E-03	0.62	6.1	0.12	0.65	30
R(RQ)(RQ)(RQ)	2.34E+03	4.7E-07	35	1.36	1.38E-04	0.79	3.5	2.59E-03	0.62	6.2	0.12	0.65	20
R(RQ)(RQ)(RQ)	1.23E+03	3.1E-07	36	1.48	1.49E-04	0.78	3.4	2.60E-03	0.63	6.2	0.12	0.64	10

pO ₂ (Pa)	R _{el} (Ω.cm)	R ₁ (Ω.cm ²)	R ₂ (Ω.cm ²)	R ₃ (Ω.cm ²)	R _{pool} (Ω.cm ²)
1.07E-19	10049	3.0	17	24	45
4.09E-20	10877	6.9	14	27	48
1.46E-20	11418	5.9	15	27	48
4.85E-21	11679	6.2	15	27	49
1.47E-21	11960	6.0	16	27	49
4.06E-22	12223	6.5	15	28	49

Temperature dependency

pH₂ 9.90E+04 Pa
 pH₂O 2.34E+03 Pa

CDC	T (°C)	ChiSq	R _{tot} (Ω)	R ₁ (Ω)	Q ₁ (Ω ⁻¹ .s ⁿ)	n ₁	R ₂ (Ω)	Q ₂ (Ω ⁻¹ .s ⁿ)	n ₂	R ₃ (Ω)	Q ₃ (Ω ⁻¹ .s ⁿ)	n ₃
R(RQ)(RQ)(RQ)	652	6.55E-07	42	1.43	8.2E-05	0.88	7.2	4.52E-03	0.41	7.05	0.19	0.63
R(RQ)(RQ)(RQ)	702	4.01E-07	23	6.06	2.9E-03	0.30	2.1	0.16	0.69	0.76	1.62	1.00
R(RQ)(RQ)(RQ)	751	1.86E-07	14	3.59	3.6E-03	0.25	1.0	0.18	0.68	0.34	1.62	0.98
R(RQ)(RQ)(RQ)	801	7.53E-08	12	0.35	6.3E-02	0.36	0.6	0.22	0.65	0.16	3.81	1.00
R(RQ)(RQ)(RQ)	848	7.18E-08	9	0.07	2.7E-02	0.67	0.4	0.21	0.63	0.18	3.57	0.99

1000/T (K ⁻¹)	R _{tot} (Ω.cm)	R ₁ (Ω.cm ²)	R ₂ (Ω.cm ²)	R ₃ (Ω.cm ²)	R _{total} (Ω.cm ²)
1.08	14216	3.2	15.8	15.6	34.5
1.03	7650	13.4	4.6	1.7	19.7
0.98	4778	7.9	2.2	0.8	10.9
0.93	4011	0.8	1.3	0.4	2.5
0.89	3058	0.1	0.8	0.4	1.4

E_A =

64.7	151.6	125.2	155.2	147.3
------	-------	-------	-------	-------

 kJ.mol⁻¹

Appendix 3 – Equivalent circuit modelling data of LSCM sintered at 1500 °C in air (sample from first batch)

Measurements as function of p_{H_2}

T 844 °C
 p_{H_2O} 2.34E+03 Pa

CDC	p_{H_2} (Pa)	ChiSq	R_{el} (Ω)	R_1 (Ω)	Q_1 ($\Omega^{-1}.s^n$)	n_1	R_2 (Ω)	Q_2 ($\Omega^{-1}.s^n$)	n_2	R_3 (Ω)	Q_3 ($\Omega^{-1}.s^n$)	n_3
R(RQ)/(RQ)/(RQ)	1.98E+04	1.4E-05	22	11	1.6E-03	0.60	224	3.1E-03	0.51	313	3.7E-02	0.94
R(RQ)/(RQ)/(RQ)	3.96E+04	3.2E-06	35	8	5.5E-03	0.41	182	2.5E-03	0.54	307	3.2E-02	0.88
R(RQ)/(RQ)/(RQ)	5.94E+04	4.3E-06	31	18	3.0E-03	0.21	164	2.5E-03	0.55	282	3.2E-02	0.88
R(RQ)/(RQ)/(RQ)	7.92E+04	2.6E-06	24	28	1.1E-03	0.19	156	2.5E-03	0.56	270	3.2E-02	0.86
R(RQ)/(RQ)/(RQ)	9.90E+04	8.5E-06	21	33	4.5E-04	0.22	151	2.4E-03	0.57	272	3.1E-02	0.84

p_{O_2} (Pa)	R_{rel} ($\Omega.cm$)	R_1 ($\Omega.cm^2$)	R_2 ($\Omega.cm^2$)	R_3 ($\Omega.cm^2$)	R_{pol} ($\Omega.cm^2$)
1.18E-14	6536	21	427	594	1042
2.95E-15	10283	15	345	584	944
1.31E-15	9160	34	312	535	881
7.38E-16	7005	54	297	513	863
4.73E-16	6049	63	286	516	866

T 644 °C
 p_{H_2O} 2.34E+03 Pa

CDC	p_{H_2} (Pa)	ChiSq	R_{el} (Ω)	R_1 (Ω)	Q_1 ($\Omega^{-1}.s^n$)	n_1	R_2 (Ω)	Q_2 ($\Omega^{-1}.s^n$)	n_2	R_3 (Ω)	Q_3 ($\Omega^{-1}.s^n$)	n_3
R(RQ)/(RQ)/(RQ)	1.98E+04	8.9E-05	101	34	1.3E-04	1.00	522	1.1E-03	0.72	4315	1.1E-03	0.47
R(RQ)/(RQ)/(RQ)	3.96E+04	9.3E-06	115	43	2.4E-04	0.86	1182	5.9E-04	0.66	7848	1.6E-03	0.44
R(RQ)/(RQ)/(RQ)	5.94E+04	6.1E-06	123	38	2.0E-04	0.89	1376	5.4E-04	0.65	9107	1.7E-03	0.44
R(RQ)/(RQ)/(RQ)	7.92E+04	2.1E-05	127	40	1.9E-04	0.90	1441	5.3E-04	0.65	25652	1.9E-03	0.41
R(RQ)/(RQ)/(RQ)	9.90E+04	9.7E-06	130	39	2.0E-04	0.89	1513	5.2E-04	0.64	38874	2.0E-03	0.41

p_{O_2} (Pa)	R_{rel} ($\Omega.cm$)	R_1 ($\Omega.cm^2$)	R_2 ($\Omega.cm^2$)	R_3 ($\Omega.cm^2$)	R_{pol} ($\Omega.cm^2$)
2.90E-20	29655	64	993	8201	9258
7.26E-21	33675	81	2246	14917	17244
3.22E-21	36077	72	2615	17309	19996
1.81E-21	37118	75	2738	48755	51569
1.16E-21	38149	74	2875	73885	76834

Measurements as function of pH₂O

T 851 °C
pH₂ 8.14E+04 Pa

CDC	pH ₂ O (Pa)	ChiSq	R _{rel} (Ω)	R ₁ (Ω)	Q ₁ (Ω ⁻¹ .s ⁿ)	n ₁	R ₂ (Ω)	Q ₂ (Ω ⁻¹ .s ⁿ)	n ₂	T _{H₂O} (°C)
R(RQ)(RQ)Q	1.99E+04	6.3E-06	52	435	1.7E-03	0.46	744	2.9E-02	0.77	60
R(RQ)(RQ)Q	1.23E+04	2.4E-06	65	79	2.4E-03	0.67	1803	4.9E-03	0.35	50
R(RQ)(RQ)Q	7.37E+03	2.4E-06	71	68	2.2E-03	0.72	1151	4.7E-03	0.36	40
R(RQ)(RQ)Q	4.24E+03	3.8E-06	77	75	2.2E-03	0.71	1013	4.7E-03	0.37	30
R(RQ)(RQ)Q	2.34E+03	1.6E-05	83	85	2.1E-03	0.70	848	4.9E-03	0.38	20
R(RQ)(RQ)Q	1.23E+03	5.4E-06	87	90	2.1E-03	0.70	785	4.8E-03	0.39	10

pO ₂ (Pa)	R _{rel} (Ω.cm)	R ₁ (Ω.cm ²)	R ₂ (Ω.cm ²)	R _{pool} (Ω.cm ²)
6.94E-14	15338	827	1414	2241
2.66E-14	19113	149	3427	3576
9.52E-15	20806	130	2188	2317
3.15E-15	22515	142	1925	2067
9.57E-16	24339	162	1611	1772
2.64E-16	25555	171	1491	1663

T 648 °C
pH₂ 8.14E+04 Pa

CDC	pH ₂ O (Pa)	ChiSq	R _{rel} (Ω)	R ₁ (Ω)	Q ₁ (Ω ⁻¹ .s ⁿ)	n ₁	R ₂ (Ω)	Q ₂ (Ω ⁻¹ .s ⁿ)	n ₂	Q ₃ (Ω ⁻¹ .s ⁿ)	n ₃	T _{H₂O} (°C)
R(RQ)(RQ)Q	1.99E+04	2.8E-05	134	4334	9.9E-04	0.43	790	1.4E-03	0.67	4.5E-02	1.00	60
R(RQ)(RQ)Q	1.23E+04	5.5E-05	148	3851	5.9E-04	0.49	80	4.6E-03	1.00	3.4E-02	1.00	50
R(RQ)(RQ)Q	7.37E+03	3.0E-05	148	3813	5.6E-04	0.49	89	4.2E-03	1.00	3.2E-02	1.00	40
R(RQ)(RQ)Q	4.24E+03	3.0E-05	151	3835	5.5E-04	0.49	93	3.6E-03	1.00	3.2E-02	1.00	30
R(RQ)(RQ)Q	2.34E+03	5.5E-04	155	3159	6.7E-04	0.47	500	1.6E-03	0.74	1.5E-02	0.81	20
R(RQ)(RQ)Q	1.23E+03	5.1E-06	187	29	1.9E-04	0.91	2722	4.0E-04	0.57	8.4E-03	0.74	10

pO ₂ (Pa)	R _{rel} (Ω.cm)	R ₁ (Ω.cm ²)	R ₂ (Ω.cm ²)	R _{pool} (Ω.cm ²)
1.68E-19	39203	8237	1501	9738
6.44E-20	43176	7319	152	7471
2.30E-20	43340	7247	169	7416
7.62E-21	44053	7290	177	7467
2.31E-21	45179	6004	950	6954
6.38E-22	54825	56	5173	5229

Temperature dependency

pH₂ 9.90E+04 Pa
 pH₂O 2.34E+03 Pa

CDC	T (°C)	ChiSq	R _{el} (Ω)	R ₁ (Ω)	Q ₁ (Ω ⁻¹ .s ⁿ)	n ₁	R ₂ (Ω)	Q ₂ (Ω ⁻¹ .s ⁿ)	n ₂
R(RQ)(RQ)	700	1.41E-04	223	1231	8.2E-04	0.54	1685	4.8E-02	1.00
R(RQ)(RQ)	750	4.46E-05	137	537	1.1E-03	0.57	1150	3.6E-02	0.93
R(RQ)(RQ)	808	2.50E-05	75	238	1.7E-03	0.60	529	3.3E-02	0.82
R(RQ)(RQ)	857	1.10E-05	49	126	2.3E-03	0.61	226	3.3E-02	0.75

1000/T (K ⁻¹)	R _{el} (Ω.cm)	R ₁ (Ω.cm ²)	R ₂ (Ω.cm ²)	R _{pol} (Ω.cm ²)
1.03	65076	2340	3203	5544
0.98	40195	1020	2185	3205
0.93	22007	452	1006	1459
0.90	14361	240	430	670

E_A= 93.0 138.6 122.1 128.4 kJ.mol⁻¹

Appendix 4 – Equivalent circuit modelling data of LSCM sintered at 1500 °C in air (sample from second batch)

Measurements as function of $p\text{H}_2$

T 838 °C
 $p\text{H}_2\text{O}$ 2.34E+03 Pa

CDC	$p\text{H}_2$ (Pa)	ChiSq	R_{air} (Ω)	R_1 (Ω)	Q_1 ($\Omega^{-1}\cdot\text{s}^n$)	n_1	R_2 (Ω)	Q_2 ($\Omega^{-1}\cdot\text{s}^n$)	n_2	R_3 (Ω)	Q_3 ($\Omega^{-1}\cdot\text{s}^n$)	n_3
R(RQ)(RQ)(RQ)	1.98E+04	4.0E-05	11.5	5.1	6.0E-03	0.60	212	4.7E-03	0.61	218	1.9E-02	0.90
R(RQ)(RQ)(RQ)	3.96E+04	1.9E-06	15.1	3.4	6.5E-03	0.54	197	4.0E-03	0.60	232	1.3E-02	0.83
R(RQ)(RQ)(RQ)	5.94E+04	1.9E-06	17.0	4.4	8.8E-03	0.43	200	4.1E-03	0.59	216	1.4E-02	0.84
R(RQ)(RQ)(RQ)	7.92E+04	2.2E-06	17.2	12.2	2.7E-02	0.23	195	4.1E-03	0.61	263	1.2E-02	0.85
R(RQ)(RQ)(RQ)	9.90E+04	2.4E-06	17.8	15.2	3.0E-02	0.19	184	4.2E-03	0.60	266	1.1E-02	0.85

$p\text{O}_2$ (Pa)	R_{air} ($\Omega\cdot\text{cm}$)	R_1 ($\Omega\cdot\text{cm}^2$)	R_2 ($\Omega\cdot\text{cm}^2$)	R_3 ($\Omega\cdot\text{cm}^2$)	R_{pol} ($\Omega\cdot\text{cm}^2$)
8.90E-15	3914	11	467	481	959
2.23E-15	5138	8	434	512	963
9.89E-16	5777	10	441	477	927
5.56E-16	5850	27	430	579	1036
3.56E-16	6033	33	406	586	1025

T 644 °C
 $p\text{H}_2\text{O}$ 2.34E+03 Pa

CDC	$p\text{H}_2$ (Pa)	ChiSq	R_{air} (Ω)	R_1 (Ω)	Q_1 ($\Omega^{-1}\cdot\text{s}^n$)	n_1	R_2 (Ω)	Q_2 ($\Omega^{-1}\cdot\text{s}^n$)	n_2	R_3 (Ω)	Q_3 ($\Omega^{-1}\cdot\text{s}^n$)	n_3	R_4 (Ω)	Q_4 ($\Omega^{-1}\cdot\text{s}^n$)	n_4
R(RQ)(RQ)(RQ)(RQ)	1.98E+04	1.8E-04	6.7	22.2	2.6E-05	0.50	2.9	6.0E-04	0.96	3194	6.8E-03	1.00	2090	8.8E-04	0.66
R(RQ)(RQ)(RQ)(RQ)	3.96E+04	1.9E-05	11.0	23.9	1.1E-05	0.59	3.1	5.4E-04	0.94	9957	1.3E-03	0.66	819	1.3E-03	0.70
R(RQ)(RQ)(RQ)(RQ)	5.94E+04	2.1E-05	10.5	27.5	6.7E-06	0.62	2.5	4.3E-04	1.00	10376	1.2E-03	0.66	752	1.4E-03	0.70
R(RQ)(RQ)(RQ)(RQ)	7.92E+04	2.2E-05	19.6	20.5	6.1E-06	0.69	2.4	4.2E-04	1.00	10622	1.1E-03	0.66	703	1.5E-03	0.69
R(RQ)(RQ)(RQ)(RQ)	9.90E+04	1.9E-05	20.6	21.3	5.0E-06	0.71	2.3	4.1E-04	1.00	10756	1.1E-03	0.66	712	1.6E-03	0.68

$p\text{O}_2$ (Pa)	R_{air} ($\Omega\cdot\text{cm}$)	R_1 ($\Omega\cdot\text{cm}^2$)	R_2 ($\Omega\cdot\text{cm}^2$)	R_3 ($\Omega\cdot\text{cm}^2$)	R_4 ($\Omega\cdot\text{cm}^2$)	R_{pol} ($\Omega\cdot\text{cm}^2$)
2.90E-20	2284	49	6.4	7045	4611	11712
7.26E-21	3740	53	6.8	21963	1807	23829
3.22E-21	3558	61	5.4	22887	1659	24612
1.81E-21	6634	45	5.2	23430	1550	25031
1.16E-21	6976	47	5.0	23725	1571	25348

Measurements as function of $p\text{H}_2\text{O}$ at $650\text{ }^\circ\text{C}$ and temperature dependency data

T 844 $^\circ\text{C}$
 $p\text{H}_2$ 8.14E+04 Pa

CDC	$p\text{H}_2\text{O}$ (Pa)	ChiSq	R_{tot} (Ω)	R_1 (Ω)	Q_1 ($\Omega^{-1}\cdot\text{s}^n$)	n_1	R_2 (Ω)	Q_2 ($\Omega^{-1}\cdot\text{s}^n$)	n_2	R_3 (Ω)	Q_3 ($\Omega^{-1}\cdot\text{s}^n$)	n_3	T_{1120} ($^\circ\text{C}$)
R(RQ)(RQ)(RQ)	1.99E+04	8.4E-07	12	8	1.2E-02	0.47	155	4.6E-03	0.63	352	1.1E-02	0.84	60
R(RQ)(RQ)(RQ)	1.23E+04	1.8E-06	14	13	1.8E-02	0.36	183	4.0E-03	0.64	303	1.4E-02	0.89	50
R(RQ)(RQ)(RQ)	7.37E+03	1.3E-06	15	23	2.3E-02	0.30	179	3.9E-03	0.65	290	1.5E-02	0.90	40
R(RQ)(RQ)(RQ)	4.24E+03	1.0E-06	16	23	2.1E-02	0.30	181	3.8E-03	0.66	282	1.5E-02	0.91	30
R(RQ)(RQ)(RQ)	2.34E+03	1.3E-06	17	28	2.1E-02	0.30	181	3.8E-03	0.66	275	1.4E-02	0.91	20
R(RQ)(RQ)(RQ)	1.23E+03	1.9E-06	21	60	1.8E-02	0.32	145	4.2E-03	0.69	270	1.2E-02	0.89	10

$p\text{O}_2$ (Pa)	R_{tot} ($\Omega\cdot\text{cm}$)	R_1 ($\Omega\cdot\text{cm}^2$)	R_2 ($\Omega\cdot\text{cm}^2$)	R_3 ($\Omega\cdot\text{cm}^2$)	R_{pol} ($\Omega\cdot\text{cm}^2$)
5.06E-14	4150	18	341	776	1135
1.94E-14	4708	28	405	669	1102
6.93E-15	4966	50	395	639	1084
2.29E-15	5286	50	398	622	1071
6.97E-16	5856	61	400	607	1068
1.92E-16	7029	133	321	595	1049

$p\text{H}_2$ 9.90E+04 Pa
 $p\text{H}_2\text{O}$ 2.34E+03 Pa

CDC	T ($^\circ\text{C}$)	ChiSq	R_{tot} (Ω)	R_1 (Ω)	Q_1 ($\Omega^{-1}\cdot\text{s}^n$)	n_1	R_2 (Ω)	Q_2 ($\Omega^{-1}\cdot\text{s}^n$)	n_2	R_3 (Ω)	Q_3 ($\Omega^{-1}\cdot\text{s}^n$)	n_3	R_4 (Ω)	Q_4 ($\Omega^{-1}\cdot\text{s}^n$)	n_4
R(RQ)(RQ)(RQ)	650	3.9E-06	26	99	2.1E-06	0.77	-	-	-	163	1.6E-02	1.00	13877	6.9E-04	0.55
R(RQ)(RQ)(RQ)	701	1.1E-05	21	50	1.4E-06	0.82	-	-	-	214	9.4E-03	0.93	7247	1.2E-03	0.52
R(RQ)(RQ)(RQ)(RQ)	751	1.3E-06	19	24	8.0E-07	0.89	27	3.3E-03	0.50	1216	1.0E-02	0.85	1078	1.8E-03	0.61
R(RQ)(RQ)(RQ)	801	1.8E-06	26	316	1.3E-02	0.31	-	-	-	639	8.8E-03	0.82	257	3.6E-03	0.66
R(RQ)(RQ)(RQ)	844	6.1E-06	17	9	8.8E-03	0.46	-	-	-	81	5.5E-03	0.62	472	5.8E-03	0.75

$1000/T$ (K^{-1})	R_{tot} ($\Omega\cdot\text{cm}$)	R_1 ($\Omega\cdot\text{cm}^2$)	R_2 ($\Omega\cdot\text{cm}^2$)	R_3 ($\Omega\cdot\text{cm}^2$)	R_4 ($\Omega\cdot\text{cm}^2$)	R_{pol} ($\Omega\cdot\text{cm}^2$)
1.08	8943	218	-	359	30610	31187
1.03	7121	109	-	472	15986	16567
0.98	6501	54	59	2681	2378	5172
0.93	8855	696	-	1409	567	2673
0.90	5841	19	-	178	1041	1239

EA= 10.8 48.2 - 0.0 177.7 143.3 $\text{kJ}\cdot\text{mol}^{-1}$

Appendix 5 – Equivalent circuit modelling data of LSCM sintered at 1200 °C in hydrogen

Measurements as function of p_{H_2}

T 834 °C
 p_{H_2O} 2.34E+03 Pa

CDC	p_{H_2} (Pa)	ChiSq	R_{el} (Ω)	R_1 (Ω)	Q_1 ($\Omega^{-1}.s^n$)	n_1	R_2 (Ω)	Q_2 ($\Omega^{-1}.s^n$)	n_2
R(RQ)(RQ)	1.98E+04	3.2E-06	107	32	1.1E-03	0.45	28	2.0E-03	0.90
R(RQ)(RQ)	3.96E+04	2.4E-06	128	39	9.3E-04	0.45	26	1.7E-03	0.91
R(RQ)(RQ)	5.94E+04	2.5E-06	142	44	9.0E-04	0.44	25	1.6E-03	0.90
R(RQ)(RQ)	7.92E+04	2.6E-06	154	46	8.3E-04	0.45	25	1.5E-03	0.90
R(RQ)(RQ)	9.90E+04	2.1E-06	166	46	6.7E-04	0.48	27	1.4E-03	0.90

p_{O_2} (Pa)	R_{el} ($\Omega.cm$)	R_1 ($\Omega.cm^2$)	R_2 ($\Omega.cm^2$)	R_{pol} ($\Omega.cm^2$)
7.33E-15	36274	71	61	132
1.83E-15	43478	85	57	142
8.14E-16	48151	96	55	151
4.58E-16	52201	102	56	158
2.93E-16	56496	101	59	160

T 647 °C
 p_{H_2O} 2.34E+03 Pa

CDC	p_{H_2} (Pa)	ChiSq	R_{el} (Ω)	R_1 (Ω)	Q_1 ($\Omega^{-1}.s^n$)	n_1	R_2 (Ω)	Q_2 ($\Omega^{-1}.s^n$)	n_2	R_3 (Ω)	Q_3 ($\Omega^{-1}.s^n$)	n_3
R(RQ)(RQ)(RQ)	1.98E+04	1.5E-06	214	68	1.7E-03	0.43	74	3.0E-03	0.67	132	5.2E-03	0.88
R(RQ)(RQ)	3.96E+04	3.1E-06	267	-	-	-	118	1.3E-03	0.56	160	3.8E-03	0.86
R(RQ)(RQ)	5.94E+04	2.2E-06	294	-	-	-	133	1.2E-03	0.55	163	3.7E-03	0.88
R(RQ)(RQ)	7.92E+04	3.1E-06	316	-	-	-	130	1.1E-03	0.57	178	3.5E-03	0.87
R(RQ)(RQ)	9.90E+04	2.6E-06	336	-	-	-	139	1.1E-03	0.56	180	3.5E-03	0.87

p_{O_2} (Pa)	R_{el} ($\Omega.cm$)	R_1 ($\Omega.cm^2$)	R_2 ($\Omega.cm^2$)	R_3 ($\Omega.cm^2$)	R_{pol} ($\Omega.cm^2$)
3.64E-20	72789	150	163	290	603
9.10E-21	90634	-	259	353	612
4.04E-21	99637	-	293	360	653
2.28E-21	107358	-	288	393	681
1.46E-21	113871	-	308	398	705

Measurements as function of p_{H_2O}

T 834 °C
 p_{H_2} 8.14E+04 Pa

CDC	p_{H_2O} (Pa)	ChiSq	R_{tot} (Ω)	R_1 (Ω)	Q_1 ($\Omega^{-1} \cdot s^n$)	n_1	R_2 (Ω)	Q_2 ($\Omega^{-1} \cdot s^n$)	n_2	T_{H_2O} (°C)
R(RQ)/(RQ)	1.99E+04	3.1E-06	72	15	2.5E-03	0.90	23	1.3E-03	0.48	60
R(RQ)/(RQ)	1.23E+04	2.5E-06	80	16	2.1E-03	0.90	25	1.2E-03	0.48	50
R(RQ)/(RQ)	7.37E+03	2.4E-06	86	18	1.9E-03	0.91	27	1.1E-03	0.49	40
R(RQ)/(RQ)	4.24E+03	2.7E-06	91	20	1.8E-03	0.90	28	1.1E-03	0.49	30
R(RQ)/(RQ)	2.34E+03	2.6E-06	95	21	1.8E-03	0.90	31	1.1E-03	0.48	20
R(RQ)/(RQ)	1.23E+03	5.9E-06	100	21	1.8E-03	0.91	35	1.2E-03	0.45	10

pO_2 (Pa)	R_{tot} ($\Omega \cdot cm$)	R_1 ($\Omega \cdot cm^2$)	R_2 ($\Omega \cdot cm^2$)	$R_{p_{pol}}$ ($\Omega \cdot cm^2$)
3.14E-14	24441	32	51	83
1.20E-14	27189	36	56	92
4.30E-15	29259	40	59	99
1.42E-15	30728	43	62	105
4.32E-16	32230	46	67	113
1.19E-16	33895	46	77	123

T 648 °C
 p_{H_2} 8.14E+04 Pa

CDC	p_{H_2O} (Pa)	ChiSq	R_{tot} (Ω)	R_1 (Ω)	Q_1 ($\Omega^{-1} \cdot s^n$)	n_1	R_2 (Ω)	Q_2 ($\Omega^{-1} \cdot s^n$)	n_2	T_{H_2O} (°C)
R(RQ)/(RQ)	1.99E+04	7.8E-06	202	75	1.5E-03	0.58	146	3.0E-03	0.82	60
R(RQ)/(RQ)	1.23E+04	6.9E-06	265	100	1.2E-03	0.58	165	3.3E-03	0.84	50
R(RQ)/(RQ)	7.37E+03	3.5E-06	251	102	1.3E-03	0.58	175	3.2E-03	0.84	40
R(RQ)/(RQ)	4.24E+03	2.8E-06	259	119	1.3E-03	0.56	174	3.4E-03	0.86	30
R(RQ)/(RQ)	2.34E+03	2.9E-06	267	124	1.3E-03	0.56	181	3.3E-03	0.86	20
R(RQ)/(RQ)	1.23E+03	8.0E-06	271	174	1.4E-03	0.44	184	3.4E-03	0.86	10

pO_2 (Pa)	R_{tot} ($\Omega \cdot cm$)	R_1 ($\Omega \cdot cm^2$)	R_2 ($\Omega \cdot cm^2$)	$R_{p_{pol}}$ ($\Omega \cdot cm^2$)
1.68E-19	68469	166	323	488
6.44E-20	90095	221	363	584
2.30E-20	85096	225	387	611
7.62E-21	88035	263	383	645
2.31E-21	90679	273	400	672
6.38E-22	92081	384	406	790

Temperature dependency

pH₂ 9.90E+04 Pa
 pH₂O 2.34E+03 Pa

CDC	T (°C)	ChiSq	R _{g1} (Ω)	R ₁ (Ω)	Q ₁ (Ω ⁻¹ .s ⁿ)	n ₁	R ₂ (Ω)	Q ₂ (Ω ⁻¹ .s ⁿ)	n ₂
R(RQ)(RQ)	652	2.0E-06	383	165	1.0E-03	0.56	420	1.9E-03	0.82
R(RQ)(RQ)	702	5.2E-06	213	91	1.1E-03	0.55	151	2.3E-03	0.84
R(RQ)(RQ)	752	6.6E-06	126	61	1.3E-03	0.44	60	2.5E-03	0.85
R(RQ)(RQ)	799	3.8E-06	89	26	2.9E-03	0.87	36	1.3E-03	0.47
R(RQ)(RQ)	835	2.4E-06	66	13	3.6E-03	0.91	23	1.5E-03	0.48

1000/T (K ⁻¹)	R _{g1} (Ω.cm)	R ₁ (Ω.cm ²)	R ₂ (Ω.cm ²)	R _{pot} (Ω.cm ²)
1.08	129828	365	927	1292
1.03	72246	200	334	534
0.98	42721	134	133	267
0.93	30039	57	79	136
0.90	22271	29	51	80

E_A= 80.7 113.9 133.3 126.6 kJ.mol⁻¹

Appendix 6 – Equivalent circuit modelling data of gold paste covered LSCM sintered at 1200 °C in air

Measurements as function of $p\text{H}_2$

T 849 °C
pH₂O 2.34E+03 Pa

CDC	pH ₂ (Pa)	ChiSq	R _{hel} (Ω)	R ₁ (Ω)	Q ₁ (Ω ⁻¹ .s ⁿ)	n ₁	R ₂ (Ω)	Q ₂ (Ω ⁻¹ .s ⁿ)	n ₂	R ₃ (Ω)	Q ₃ (Ω ⁻¹ .s ⁿ)	n ₃	L (Ωs)
LR(RQ)(RQ)(RQ)	1.98E+04	1.9E-06	0.12	7.0E-02	0.21	0.55	5.1E-02	0.69	0.83	0.39	5.22	0.97	2.6E-07
LR(RQ)(RQ)(RQ)	3.96E+04	9.0E-07	0.14	9.6E-02	0.19	0.54	2.4E-02	0.81	0.91	0.33	5.86	0.97	2.3E-07
LR(RQ)(RQ)(RQ)	5.94E+04	1.0E-06	0.15	1.1E-01	0.19	0.55	1.2E-02	0.88	1.00	0.27	6.43	0.97	2.0E-07
LR(RQ)(RQ)(RQ)	7.92E+04	2.2E-06	0.15	1.2E-01	0.18	0.55	9.2E-03	0.89	1.00	0.22	7.00	0.96	1.7E-07
LR(RQ)(RQ)(RQ)	9.90E+04	3.8E-06	0.15	1.2E-01	0.17	0.55	1.4E-02	0.79	0.87	0.17	7.66	0.95	1.5E-07

pO ₂ (Pa)	R _{hel} (Ω.cm)	R ₁ (Ω.cm ²)	R ₂ (Ω.cm ²)	R ₃ (Ω.cm ²)	R _{pol} (Ω.cm ²)
1.48E-14	42	0.15	0.11	0.85	1.12
3.71E-15	46	0.21	0.05	0.72	0.98
1.65E-15	52	0.24	0.03	0.60	0.87
9.27E-16	52	0.26	0.02	0.49	0.77
5.94E-16	52	0.26	0.03	0.38	0.67

T 650 °C
pH₂O 2.34E+03 Pa

CDC	pH ₂ (Pa)	ChiSq	R _{hel} (Ω)	R ₁ (Ω)	Q ₁ (Ω ⁻¹ .s ⁿ)	n ₁	R ₂ (Ω)	Q ₂ (Ω ⁻¹ .s ⁿ)	n ₂	R ₃ (Ω)	Q ₃ (Ω ⁻¹ .s ⁿ)	n ₃	R ₄ (Ω)	Q ₄ (Ω ⁻¹ .s ⁿ)	n ₄
R(RQ)(RQ)(RQ)(RQ)	1.98E+04	4.6E-06	0.59	0.25	3.1E-03	0.70	1.23	0.14	0.41	1.23	0.65	0.75	0.76	4.39	1.00
R(RQ)(RQ)(RQ)(RQ)	3.96E+04	2.8E-06	0.59	0.31	3.0E-03	0.68	1.22	0.10	0.46	1.01	0.60	0.77	0.54	4.44	1.00
R(RQ)(RQ)(RQ)(RQ)	5.94E+04	2.0E-06	0.60	0.33	2.8E-03	0.68	1.27	0.08	0.48	0.84	0.60	0.78	0.44	4.32	1.00
R(RQ)(RQ)(RQ)(RQ)	7.92E+04	1.7E-06	0.60	0.35	2.8E-03	0.67	1.31	0.07	0.50	0.72	0.60	0.80	0.38	4.03	1.00
R(RQ)(RQ)(RQ)(RQ)	9.90E+04	1.3E-06	0.61	0.34	2.3E-03	0.69	1.42	0.07	0.49	0.54	0.64	0.84	0.36	3.19	1.00

pO ₂ (Pa)	R _{hel} (Ω.cm)	R ₁ (Ω.cm ²)	R ₂ (Ω.cm ²)	R ₃ (Ω.cm ²)	R ₄ (Ω.cm ²)	R _{pol} (Ω.cm ²)
4.56E-20	199	0.55	2.71	2.72	1.67	7.7
1.14E-20	202	0.68	2.69	2.22	1.18	6.8
5.07E-21	204	0.73	2.81	1.85	0.97	6.4
2.86E-21	205	0.78	2.88	1.59	0.83	6.1
1.83E-21	208	0.74	3.13	1.18	0.80	5.9

Measurements as function of pH₂O

T 849 °C
pH₂ 8.14E+04 Pa

CDC	pH ₂ O (Pa)	ChiSq	R _{rel} (Ω)	R ₁ (Ω)	Q ₁ (Ω ⁻¹ .s ⁿ)	n ₁	R ₂ (Ω)	Q ₂ (Ω ⁻¹ .s ⁿ)	n ₂	R ₃ (Ω)	Q ₃ (Ω ⁻¹ .s ⁿ)	n ₃	T _{H2O} (°C)
R(RQ)(RQ)(RQ)	1.99E+04	2.11E-06	0.18	1.4E-02	7.1E-02	0.82	6.8E-02	0.51	0.67	5.2E-02	7.45	0.97	60
R(RQ)(RQ)(RQ)	1.23E+04	5.61E-06	0.19	9.8E-03	2.1E-02	0.92	9.0E-02	0.56	0.58	6.9E-02	7.35	0.98	50
R(RQ)(RQ)(RQ)	7.37E+03	1.04E-05	0.19	9.7E-03	5.2E-03	1.00	9.9E-02	0.57	0.55	8.3E-02	7.30	0.98	40
R(RQ)(RQ)(RQ)	4.24E+03	1.01E-05	0.20	1.1E-02	3.4E-03	1.00	1.0E-01	0.56	0.54	1.0E-01	7.18	0.98	30
R(RQ)(RQ)(RQ)	2.34E+03	5.93E-06	0.21	1.4E-02	3.5E-03	0.99	1.0E-01	0.53	0.54	1.4E-01	7.02	0.97	20
R(RQ)(RQ)(RQ)	1.23E+03	5.93E-06	0.21	1.7E-02	4.2E-03	0.95	9.6E-02	0.49	0.55	3.0E-01	7.06	0.97	10

pO ₂ (Pa)	R _{rel} (Ω.cm)	R ₁ (Ω.cm ²)	R ₂ (Ω.cm ²)	R ₃ (Ω.cm ²)	R _{pod} (Ω.cm ²)
6.35E-14	61	0.03	0.15	0.11	0.29
2.44E-14	65	0.02	0.20	0.15	0.37
8.71E-15	66	0.02	0.22	0.18	0.42
2.88E-15	68	0.02	0.23	0.23	0.48
8.75E-16	70	0.03	0.23	0.31	0.57
2.41E-16	73	0.04	0.21	0.66	0.91

T 650 °C
pH₂ 8.14E+04 Pa

CDC	pH ₂ O (Pa)	ChiSq	R _{rel} (Ω)	R ₁ (Ω)	Q ₁ (Ω ⁻¹ .s ⁿ)	n ₁	R ₂ (Ω)	Q ₂ (Ω ⁻¹ .s ⁿ)	n ₂	R ₃ (Ω)	Q ₃ (Ω ⁻¹ .s ⁿ)	n ₃	R ₄ (Ω)	Q ₄ (Ω ⁻¹ .s ⁿ)	n ₄
R(RQ)(RQ)(RQ)(RQ)	1.99E+04	2.6E-06	0.59	0.37	5.4E-03	0.63	0.95	0.15	0.47	0.58	0.59	0.79	0.54	1.70	0.99
R(RQ)(RQ)(RQ)(RQ)	1.23E+04	2.5E-06	0.59	0.47	5.8E-03	0.60	1.00	0.12	0.50	0.58	0.59	0.81	0.55	1.87	0.98
R(RQ)(RQ)(RQ)(RQ)	7.37E+03	2.2E-06	0.59	0.46	5.1E-03	0.61	1.16	0.11	0.48	0.64	0.64	0.81	0.47	2.57	0.99
R(RQ)(RQ)(RQ)(RQ)	4.24E+03	2.0E-06	0.60	0.46	4.5E-03	0.62	1.27	0.10	0.47	0.65	0.67	0.82	0.43	3.10	1.00
R(RQ)(RQ)(RQ)(RQ)	2.34E+03	1.8E-06	0.60	0.47	4.3E-03	0.62	1.33	0.10	0.47	0.68	0.67	0.81	0.41	3.55	1.00
R(RQ)(RQ)(RQ)(RQ)	1.23E+03	1.5E-06	0.62	0.39	2.7E-03	0.67	1.40	0.08	0.46	0.76	0.72	0.77	0.40	6.31	1.00

pO ₂ (Pa)	R _{rel} (Ω.cm)	R ₁ (Ω.cm ²)	R ₂ (Ω.cm ²)	R ₃ (Ω.cm ²)	R ₄ (Ω.cm ²)	R _{pod} (Ω.cm ²)
1.95E-19	200	0.81	2.10	1.28	1.19	5.38
7.49E-20	199	1.03	2.21	1.29	1.22	5.74
2.68E-20	201	1.02	2.55	1.40	1.03	6.01
8.86E-21	202	1.01	2.81	1.44	0.95	6.21
2.69E-21	203	1.03	2.93	1.50	0.91	6.37
7.42E-22	210	0.86	3.10	1.67	0.88	6.49

Temperature dependency

pH₂ 9.90E+04 Pa
pH₂O 2.34E+03 Pa

CDC	T (°C)	ChiSq	R _{el} (Ω)	R ₁ (Ω)	Q ₁ (Ω ⁻¹ .s ⁿ)	n ₁	R ₂ (Ω)	Q ₂ (Ω ⁻¹ .s ⁿ)	n ₂	R ₃ (Ω)	Q ₃ (Ω ⁻¹ .s ⁿ)	n ₃	R ₄ (Ω)	Q ₄ (Ω ⁻¹ .s ⁿ)	n ₄
R(RQ)(RQ)(RQ)(RQ)	652	6.5E-07	0.63	0.64	1.7E-03	0.66	3.80	0.02	0.58	0.46	0.06	1.00	1.03	0.86	0.80
R(RQ)(RQ)(RQ)(RQ)	701	2.8E-06	0.45	0.33	1.1E-03	0.74	0.41	0.03	0.61	1.07	0.05	0.64	0.48	1.27	0.74
R(RQ)(RQ)(RQ)(RQ)	751	2.0E-06	0.33	0.14	1.8E-03	0.77	0.59	0.12	0.48	0.09	1.80	0.79	0.12	11.06	1.00
R(RQ)(RQ)(RQ)(RQ)	798	1.6E-06	0.28	0.03	8.4E-04	1.00	0.15	0.17	0.50	0.12	0.58	0.65	0.15	8.36	0.97
LR(RQ)(RQ)(RQ)	850	3.5E-06	0.19	0.06	5.4E-01	0.43	0.04	0.58	0.76	-	-	-	0.15	7.61	0.95

with L=1.7E-07 Ω.s

pO ₂ (Pa)	R _{el} (Ω.cm)	R ₁ (Ω.cm ²)	R ₂ (Ω.cm ²)	R ₃ (Ω.cm ²)	R ₄ (Ω.cm ²)	R _{pot} (Ω.cm ²)
1.08	215	1.40	8.38	1.02	2.26	13.06
1.03	153	0.73	0.91	2.37	1.06	5.07
0.98	112	0.32	1.31	0.20	0.26	2.08
0.93	95	0.06	0.33	0.27	0.32	0.97
0.89	64	0.13	0.09	0.34	-	0.56

E_A 49.8 125.0 173.0 76.0 124.7 137.0 kJ.mol⁻¹

